Geochemistry
Geophysics
Geosystems
G3
AN ELECTRONIC JOURNAL OF THE EARTH SCIENCES
Published by AGU and the Geochemical Society

Article
Volume 5, Number 1
13 January 2004
Q01L01, doi:10.1029/2003GC000583
ISSN: 1525-2027

Steady plumes in viscously stratified, vigorously convecting, three-dimensional numerical mantle convection models with mobile plates

Julian P. Lowman
School of Earth Sciences, University of Leeds, Leeds, West Yorkshire, LS2 9JT, UK (j.lowman@earth.leeds.ac.uk)

Scott D. King
Department of Earth and Atmospheric Sciences, Purdue University, West Lafayette, IN 47907-1397, USA (sking@purdue.edu)

Carl W. Gable
Hydrology, Geochemistry and Geology (EES-6), Los Alamos National Laboratory, MS T003, Los Alamos, NM 87545, USA (gable@lanl.gov)

[1] We present results from three-dimensional (3-D) Cartesian geometry computations featuring vigorous (high Rayleigh number) mantle convection in a system incorporating stiff tectonic plates with dynamically determined, time-dependent velocities. We track plume-related hot spot motion while calculating associated synthetic hot spot tracks, allowing us to estimate plume migration rates relative to plate motion rates. Plate-like surface motion is achieved explicitly by specifying both the plate geometry and rigidity; however, plate velocities evolve dynamically in response to the buoyancy distribution within the convecting system, including buoyancy within the plate itself. We find that convection is characterized by downwelling sheets and varying numbers of 3-D upwelling structures when the lower mantle to upper mantle viscosity ratio is varied from 9 to 90. As the lower mantle viscosity is increased relative to the upper mantle viscosity, the upwellings in the calculations evolve into vigorous (active) plumes characterized by long, narrow, thermal conduits with broad, disk-like heads. The total number, shape, and persistence of the plumes are affected by the specified viscosity stratification in the calculations. Our findings indicate that hot spots associated with mantle plumes drift by smaller distances in comparable amounts of time when the lower mantle viscosity is increased relative to the upper mantle viscosity. In cases with a high lower mantle to upper mantle viscosity ratio, the depth of the flow aligned with plate motion is diminished and the plate-scale return flow is integrated into a deep, unorganized, sluggish layer. As a result, plume conduit morphology in the lower mantle of such calculations is less influenced by plate motion than in calculations with a small difference between upper mantle and lower mantle viscosity. For lower mantle viscosities 30 times and 90 times greater than the upper mantle viscosity, the lower mantle velocity field is dominated locally by active plumes anchored in the lower thermal boundary layer of the convecting system and plume migration rates are typically only about 10% of the overriding plate velocity. In such cases, we also find that plume-related hot spots persist for periods that we estimate to be between 0.55 and 1.1 plume-transit times.

Components: 13,036 words, 18 figures, 8 videos.

Keywords: mantle convection; plumes; plates; hot spot tracks; hot spots; mantle viscosity.

Index Terms: 8121 Tectonophysics: Dynamics, convection currents and mantle plumes; 8120 Tectonophysics: Dynamics of lithosphere and mantle—general; 8162 Tectonophysics: Rheology—mantle.

Received 30 May 2003; **Revised** 30 September 2003; **Accepted** 29 October 2003; **Published** 13 January 2004.

Lowman, J. P., S. D. King, and C. W. Gable (2004), Steady plumes in viscously stratified, vigorously convecting, three-dimensional numerical mantle convection models with mobile plates, *Geochem. Geophys. Geosyst.*, *5*, Q01L01, doi:10.1029/2003GC000583.

Theme: Movement, Dynamics and Geochemical Evolution of the Hawaiian Hot Spot
Guest Editors: R. Duncan, J. A. Tarduno, D. Scholl, and T. Davies

1. Introduction

[2] The determination of the mantle's radial viscosity structure [e.g., *King and Masters*, 1992; *King*, 1995; *Mitrovica*, 1996; *Mitrovica and Forte*, 1997, 2002] and the degree to which hot spots remain fixed [e.g., *Wilson*, 1963; *Morgan*, 1972, 1981; *Chase*, 1979; *Duncan*, 1981; *Molnar and Stock*, 1987; *Wessel and Kroenke*, 2000] are two long standing issues in global geophysics. Because plume motion may be directly affected by the viscosity stratification of the mantle [e.g., *Richards and Lithgow-Bertelloni*, 1996], the widely held view that hot spots are the surface expression of the impingement of deep rooted mantle plumes on the base of the lithosphere [e.g., *Morgan*, 1971, 1972; *Wilson*, 1973; *Richards et al.*, 1989; *Griffiths and Campbell*, 1990] leads to a dynamic model in which these issues are intimately connected.

[3] A well-known problem in mantle convection modeling is that plate-like surface motion is not exhibited without specifically tailoring calculations to emulate plate-like behavior [*Bercovici*, 2003; *Schubert et al.*, 2001]. For example, the inclusion of weak plate boundaries, non-Newtonian plate viscosity, and the application of a dynamically determined plate-like surface velocity field have all been used to achieve plate-like motion in mantle convection calculations [e.g., *Davies*, 1989; *Gurnis*, 1989; *King and Hager*, 1990; *Gable et al.*, 1991; *Van den Berg et al.*, 1991; *King et al.*, 1992; *Weinstein and Olson*, 1992; *Zhong and Gurnis*, 1992, 1995; *Puster et al.*, 1995; *Zhong et al.*, 1998, 2000; *Monnereau and Quéré*, 2001; *Lowman et al.*, 2001]. In order to investigate the effect of mantle viscosity stratification on plume versus plate motion, a model is required that allows plumes to evolve naturally in a system characterized by plate-like surface motion that is dynamically determined by the buoyancy field. Although it would be desirable to include rheology that allows for plate-like behavior to evolve self-consistently [e.g., *Tackley*, 1998, 2000; *Trompert and Hansen*, 1998] this degree of completeness is not required for studying the long-term coupling between plates and mantle convection. More to the point, self-consistent plate generation models have not yet reached the maturity required for studying the feedback between plate motion and mantle convection over long integration times. This work employs a force-balance method [*Gable et al.*, 1991] to model the evolving velocities of the plates in a system with a specified plate geometry. We present the results from a suite of numerical calculations that include the fundamental features required to study plume motion relative to plate motion; high Rayleigh number, 3-D, convection and mobile plates. The highly time-dependent systems are presented using a number of animations in order to gain insight into the dynamic behavior of the systems.

[4] Previous studies of plume-related hot spot fixity (or conversely, plume mobility) have generally focussed on the broader topic of mantle planform. Investigations have included both laboratory tank [*Richards and Griffiths*, 1988; *Feighner and Richards*, 1995; *Davaille*, 1999; *Jellinek and Manga*, 2002; *Gonnermann et al.*, 2002; *Davaille et al.*, 2002; *Jellinek et al.*, 2003] and numerical model studies [*Richards and Lithgow-Bertelloni*, 1996; *Steinberger and O'Connell*, 1997, 1998; *Bunge et al.*, 1997; *Richards et al.*, 1999; *Larsen et al.*, 1999; *Steinberger*, 2000; *Brunet and Yuen*, 2000]. The experiments presented can be divided

into self-consistent models, in which plumes evolve naturally from the hot thermal boundary layer that develops in the convecting flow [*Bunge et al.*, 1997; *Richards et al.*, 1999; *Larsen et al.*, 1999; *Brunet and Yuen*, 2000], and models in which plumes are introduced into a large-scale flow driven entirely by the negative buoyancy associated with the lithospheric thickening and slab driven flow that supplies the large majority of the driving force responsible for large scale mantle motion [*Richards and Lithgow-Bertelloni*, 1996; *Steinberger and O'Connell*, 1997, 1998]. Findings from earlier studies have indicated that a strong depth-dependent viscosity [*Richards and Griffiths*, 1988; *Richards and Lithgow-Bertelloni*, 1996; *Bunge et al.*, 1997; *Steinberger and O'Connell*, 1998; *Zhong et al.*, 2000] rather than temperature-dependent viscosity [*Jellinek et al.*, 2003] may play an important role in stabilizing plume positions.

[5] In this study we focus on the mean viscosity contrast required between the upper mantle and lower mantle in order to obtain steady, whole-mantle plumes. We compare the influence of plate geometry and mantle viscosity layering on plume motion in four high resolution calculations. Movement of the hottest parts of the most vigorous plumes is tracked in the upper mantle allowing determination of how an associated hot spot track would evolve on the overriding plate.

2. Model Description

[6] The nondimensional equations of motion solved in our numerical experiments have been discussed previously by *Lowman et al.* [2003]. In the calculations, time is nondimensionalized using the time-scale for thermal diffusion, d^2/κ, where κ is the thermal diffusivity and d is the depth of the convecting system. One nondimensional time unit is equivalent to one diffusion time. The nature of the flow is characterized by two independently specified nondimensional parameters, the Bénard-Rayleigh number, Ra_B [*Chandrasekhar*, 1961] and the internal heating rate, H, as well as the depth dependence of viscosity. All parameters appearing in the definition of the Rayleigh number are spatially constant with the exception of viscosity, which is depth-dependent only.

[7] The Rayleigh number, Ra_B, in our calculations, based on the lower mantle viscosity, is 1.667×10^6. The thickness of the upper thermal boundary layers and the heat flows obtained from our calculations lead us to conclude that the specified lower mantle Rayleigh number is at least a factor of two times lower than what is appropriate for the Earth, however, we must prescribe a conservative Rayleigh number in our calculations in order to ensure that they are numerically well resolved (i.e., thermal boundary layers encompass at least three layers of our numerical grid).

[8] The vigor of the upwellings in a convecting system is strongly influenced by internal heating. We specify a nondimensional heating rate, H, of 15 in all of the calculations presented. The combination of an isothermal upper and lower boundary and the constant internal heating rate employed in our calculations does not allow for an a priori specification of the internal-heating rate as a percentage of the mean surface heat flux. With this heating rate we find that, when expressed as a percentage of the mean surface heat flux, the internal heating rate falls in the 50–60% range in each of our calculations. An alternative interpretation is that these heating rates imply that the ratio of the mean heat flux across the lower boundary to the mean heat flux across the upper surface is between 0.4 and 0.5 in each calculation. Due to the difference in the surface areas of the core-mantle boundary and the Earth's surface, the ratio of the mean heat flux across the core-mantle boundary to the mean surface heat flux for the Earth (excluding crustal sources) must be 0.4 to 0.5 if 12–15% of the Earth's surface heat loss (excluding crustal sources) comes from basal heating of the mantle (i.e., the core). This range is well within currently supported values [e.g., *Buffet et al.*, 1992; *Labrosse et al.*, 1997]. Consequently, we suggest that the thermal gradients across the bases of our Cartesian geometry calculations must be similar to the radial temperature gradients found in a spherical shell mantle that is about 85% internally heated and that the plumes in our calculations will have a similar vigor to the plumes in the corresponding spherical system. The absence of a temperature dependence in viscosity means that we use the term conduit when describing

plumes to imply a thermal conduit. That is, an anomalously hot tail connecting the lower thermal boundary layer of the convecting system to the thermal constituting the plume head.

[9] We simulate tectonic plates by specifying a finite thickness viscous layer at the top of the model and prescribing piecewise uniform surface velocities. The plates in the model neither drive nor resist the convective flow (that is, the specified plate velocities do not add to or subtract from the energy of the system). This condition is achieved by continually updating the plate velocities so that the integrated shear tractions on the base of each plate vanishes at all times. Thus plate velocities evolve so that the system responds to the distribution of buoyancy within both the plate and underlying fluid. The resulting condition is consistent with a rigid plate uniformly distributing the stresses applied at its base. The plate geometry remains unchanged during the evolution of each model. The high viscosity layer at the top of the models acts as a first-order approximation for the stiffness associated with the Earth's cold lithosphere. Below this layer we specify a uniform upper mantle viscosity and a viscosity jump at 0.22d (660 km) depth. In all calculations, the plates have a nondimensional thickness of approximately 0.055d (a thickness representative of the mean thermal boundary layer thickness of calculations with the Rayleigh numbers and internal heating rate we have specified). The plate model has been compared with material property methods and power-law rheology plate generation methods and the agreement between the surface heat flux and plate velocities of these models was found to be excellent [*King et al.*, 1992].

3. Results

[10] We present the results from four 3-D calculations. To obtain a thermally equilibrated initial condition with the smallest amount of computational effort, we first determine a 2-D solution in which all parameters are specified as they will be in the subsequent 3-D calculation. (We define a thermally equilibrated temperature field as a temperature field taken from a system that is not exhibiting any long term heating or cooling.) The 2-D calculations feature a pair of equal size plates. These solutions are projected in the y-direction and both the plate geometry of the 3-D model and a random temperature perturbation are added to the resulting 3-D initial condition. To obtain a starting point for the results presented here, we integrate each of models forward from the 3-D initial conditions for a minimum of 0.01 diffusion times (amounting to several mantle overturns).

[11] An alternative representation of time which leads to a more intuitive scale for the plate velocities is obtained by considering the characteristic rise time of a plume (a plume-transit time), which is defined by the time required for a plume to traverse the depth of the convecting system. The characteristic rise velocity of a plume is given by

$$V_p = c\kappa Ra_B^{1/3}/d, \qquad (1)$$

where the empirically determined constant $c \approx 9$ [e.g., *Jellinek et al.*, 2003]. Consequently, a plume-transit time is given by d/V_p. *Jellinek et al.* [2003] showed that in a fluid with no internal heat sources or viscosity depth dependence, there is a transition from a flow dominated by ascending plume motion to a flow governed by large-scale (plate driven) motion when plate velocity is of order V_p. Accordingly, in a system incorporating plate motion, the most robust examples of plume stationarity require plate velocities above the rising plume that are at least of order V_p.

[12] On the basis of the lower mantle value of Ra_B, the duration of each of our calculations is 1.71 plume-transit times. This estimation is approximate and is affected by complicating factors like internal heating and the effectively higher Rayleigh number of the weak upper mantle in our calculations. However, observation of plume motion in Animation 1, 3, 5 and 7 (described below) indicates this value is a reasonable prediction of plume-transit times in our calculations. On the basis of this rough estimate, we present plate velocities in the remainder of this paper in terms of mantle depths per plume-transit time and hot spot lifetimes in terms of plume-transit times.

[13] Figure 1 shows map views of the two plate geometries specified in the 3-D calculations. The black region represents the calculation solution

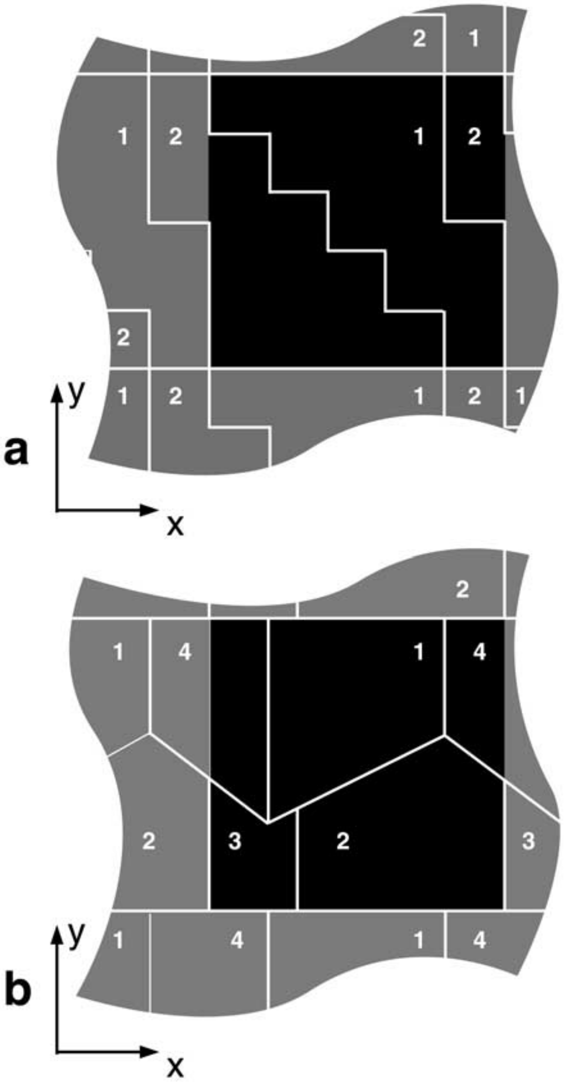

Figure 1. Plate geometries specified in the calculations. The solution domain is shown in black and the plate boundaries are shown with white lines. The gray shaded region illustrates the periodic nature of the solutions. Note that Plate 2 in Figure 1a and Plate 4 in Figure 1b wrap around the solution domain. The numeric designation of plates in this figure and the indicated x-y axes orientation provide the plate number and direction definitions referred to throughout the text and in subsequent figures and animations.

domain and the gray regions represent the repeating plate pattern implied by the periodic boundary conditions. The plate geometry in Figure 1a was found to be favorable in obtaining nearly steady plate motion. Consequently, it provides an exceptionally well-controlled experimental setup in which plume evolution is not influenced by large changes in plate motion as the calculations develop [e.g., *King et al.*, 2002; *Lowman et al.*, 2003]. Figure 1b, shows the plate geometry featured in the remaining calculations. (Note that this geometry, like the Earth, is characterized by the presence of triple junctions.) *King et al.* [2002] employed the same plate geometry in a previous study and found that calculations with a similar lower mantle to upper mantle viscosity ratio exhibited periods of relatively steady plate motion punctuated by significant plate reorganization events. However, in this study, we have chosen to examine periods between major plate reorganization events (for example, we do not examine periods that include the creation of substantial new subduction zones).

[14] Throughout the remainder of this paper we describe four calculations named using the convention Model Xa or Model Xb, where Model Xa and Model Xb feature the plate geometries shown in Figure 1a and Figure 1b, respectively, and X = 9, 30 or 90. X is the factor by which the viscosity in the model increases at a depth of $0.22d$ (660 km). We first examine plume versus plate motion in Model 30a.

[15] Animation 1 (see Figure 2 for still image) shows the evolution of the temperature field of Model 30a over a period of $1.71d/V_p$ (0.0016 diffusion times). Also shown in the animation are a pair of thumbnails of the surface plate geometry indicating a plate numbering system and plate velocity evolution. The latter is presented by using an arrow placed at the center of each plate which indicates the instantaneous plate velocity direction. The arrow lengths indicate the plate velocity magnitude. The period shown in Animation 1 starts 0.0107 diffusion times after the start of the 3-D calculation and is representative of typical flow after an initially transient period.

[16] During the period shown, the calculation features a pair of plumes (orange columnar features) rising from the lower thermal boundary of the model below Plate 2. At the end of the animation, a large plume has also formed from the coalescing of several smaller plumes below Plate 1. The blue downwelling sheets in the animation are associated with the downwelling of cold plate material at the convergent plate boundaries. Hot, orange, tube-

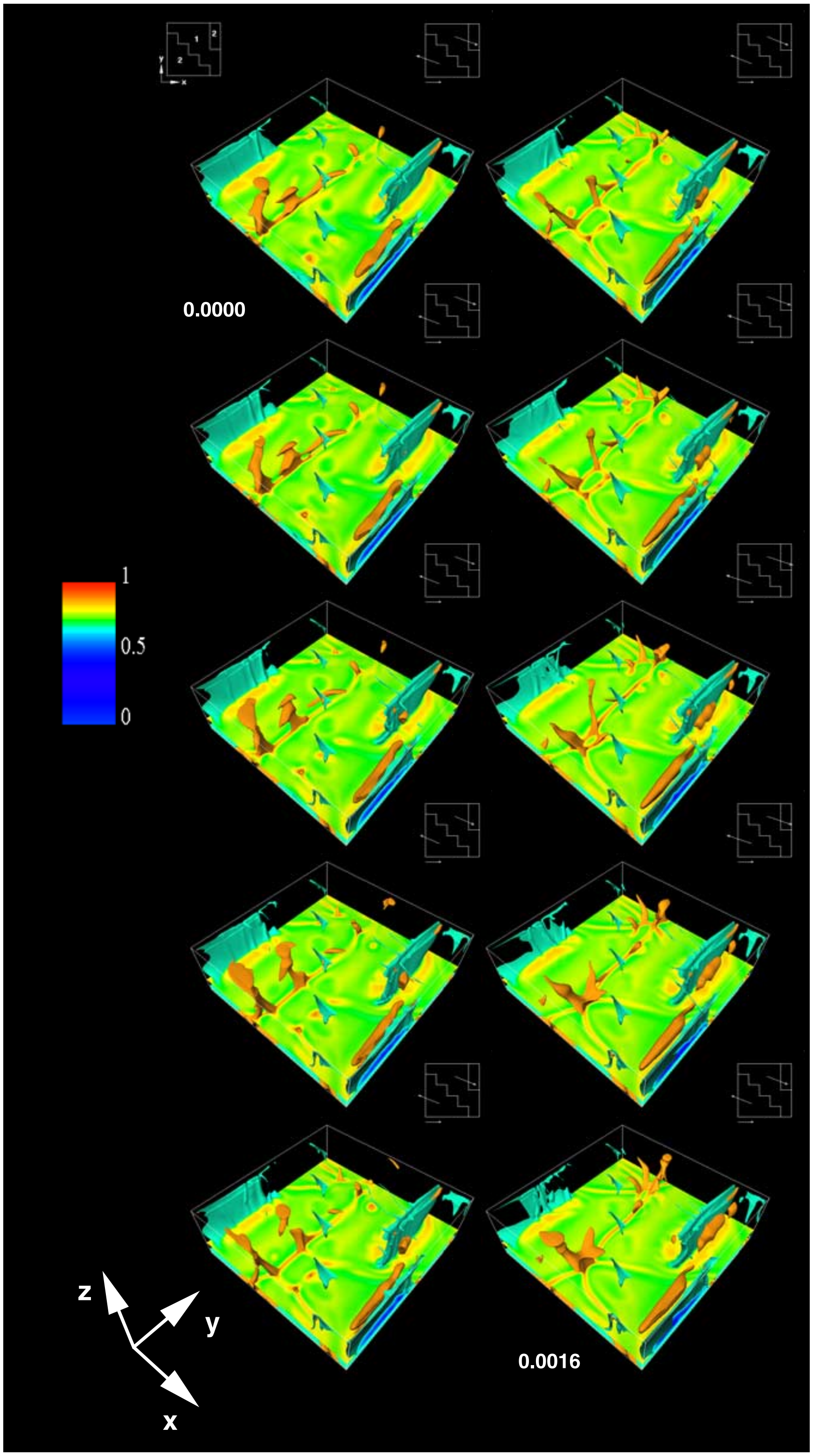
1
2
2
y
x
0.0000
1
0.5
0
z
y
x
0.0016

shaped isosurfaces can be seen lying below the youngest parts of the plates. These hot regions are juxtaposed along-side the downwelling sheets and are associated with the entrainment of hot upper mantle material by plate motion into the region around subducting plates. In these regions, buoyant material resists being dragged into the lower mantle and becomes trapped by the downward pull of the sinking plate material [*Lowman et al.*, 2001, 2003]. This heat buildup occurs in internally heated models because the upper mantle cannot sufficiently cool through conductive heat loss into the overlying plate before reaching a subduction zone. Also evident in Animation 1 are five blue downwelling sheets (lined up almost vertically in the movie frame) confined to the upper mantle. These sheets are associated with weak convergence of very young plate along the boundaries between offset sections of the divergent plate boundaries (N.B., this occurs because plate motion is not parallel to the axis of the domain.)

[17] The two plumes in Animation 1 exhibit a dynamic behavior characterized by pulsing, coalescing and thinning. However, relative to plate motion, their bases move very little. In fact, the plume-like columns persist in the same general vicinity for periods comparable to the plume-transit time while the plates move at velocities that are approximately 11 times greater than the plume migration rates. The pulsing behavior of the plumes originates deep in the system from the arrival of developing thermal boundary layer instabilities at the base of the mature thermal plume conduit [e.g., *Jarvis*, 1984; *Weinstein et al.*, 1989] rather than originating at the viscosity interface [e.g., *Van Keken et al.*, 1992; *Van Keken and Gable*, 1995].

[18] Figure 3 shows the time series of the plate velocity magnitudes for Model 30a. Arrows are attached to the velocity magnitude curve to show the corresponding plate velocity direction. The figure shows that the direction of plate motion during the interval examined is almost constant. However, plate velocity magnitude varies from about $1.30V_p$ to just over $1.65V_p$.

[19] Animation 2 (see Figure 4 for still image) is a temperature contour map on a horizontal slice through Model 30a at a depth of $0.083d$ (250 km). Temperatures between 0.0 and 0.68 are contoured in shades of blue at an interval of 0.01. Temperatures between 0.88 and 1.00 are contoured in shades of orange and red with the same interval. The two plumes that appear clearly in Animation 1 below Plate 2 are manifested in Animation 2 as a pair of large hot spots. Indeed, the combination of the slightly low Rayleigh number and the depth at which the slice is shown mean that the mushroom shaped plume heads appear as particularly large hot spots. The two dominant hot spots revealed in the animation have distinctly different life times. The more persistent exists for over $1.57d/V_p$, almost the entire duration of the depicted sequence, while the other appears for just over $0.6d/V_p$. In fact the plumes in Animation 1 clearly prevail in roughly the same location in the lower mantle for even longer durations than the hot spots shown in

Figure 2. Temperature field evolution in Model 30a. The calculation has periodic (wrap-around) boundary conditions and incorporates two plates with thicknesses of $0.052d$ (150 km). The Rayleigh number specified for the calculation (based on the lower mantle viscosity) is $Ra_B = 1.666 \times 10^6$ and the non-dimensional heating rate $H = 15$. Viscosity decreases by a factor of 30 above a depth of $0.22d$ (670 km). The blue isosurface has a temperature of 0.68 and the orange isosurface has a temperature of 0.88. The blue isosurface is cropped at a depth of $0.069d$ (200 km). The color legend indicates the colour palette used in the figure. The co-ordinate axes to the lower left indicate the orientation of the temperature field relative to other figures and animations from Model 30a. The surface plate geometry is indicated at the upper left with a numerical referencing system. Plate velocity is also shown to the upper right of each corresponding temperature field with arrows superimposed on a plate geometry planview that indicates the instantaneous direction and magnitude of plate motion above the temperature field. Arrow lengths are time-dependent and are proportional to a plate velocity magnitude of 1000d/diffusion-time, which is indicated by the length of the arrow below each plate velocity panel. The first and final panels in the sequence are indicated by start time and end time labels of 0.0000 and 0.0016 diffusion times, respectively. Panels are shown at intervals of approximately 0.000178 diffusion times. Calculations were performed on a 16 processor Beowulf cluster and require approximately 1 Gigabyte of RAM per process. Each calculation is computed on a $325 \times 325 \times 129$ node grid and models a volume with physical dimensions of $3 \times 3 \times 1$.

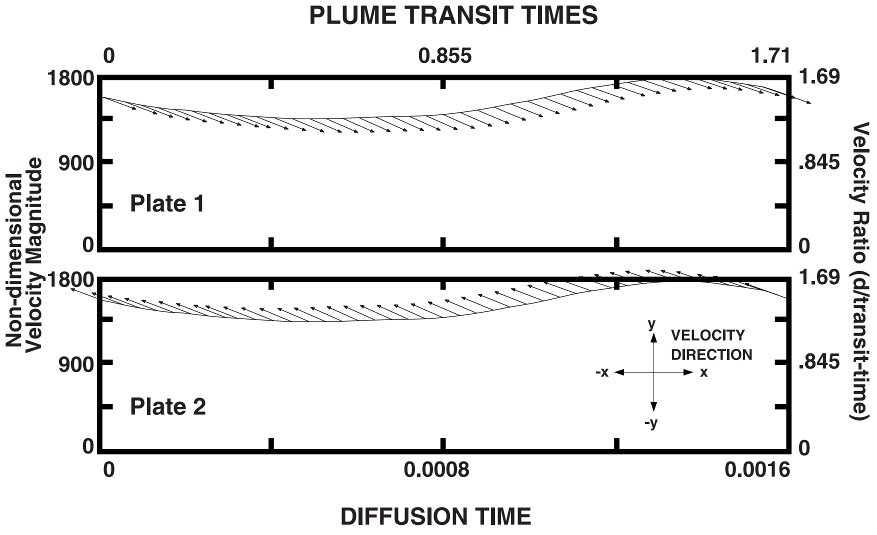

Figure 3. Plate velocity time series for Model 30a. Nondimensional plate velocity magnitude is shown in accord with the plate numbering system introduced in Figure 1. Arrows are attached to the velocity magnitude curves at an interval of 0.000032 diffusion times and show the direction of the plate motion at the corresponding instant. The time series corresponds to the period shown in Animation 1.

Animation 2. However, between long periods of stability in the upper mantle, the hot spots occasionally appear to either fizzle out or rapidly migrate over a short distance because of their pulsing and coalescing behavior.

[20] Figure 5 shows a map view at a depth of $0.083d$ (250 km) of the history of the distribution of hot spot locations (rectangles) and associated hot spot tracks (circles) as they would appear on the plate at a time corresponding to the end of the sequence shown in Animation 1 (Model 30a). The hot spot tracks (circles) are determined by calculating the trajectory end-point of a particle that moves with the velocity of the overlying plate from a time when it is released at the center of the hot spot location until time $1.71d/V_p$ (the ending of Animations 1 and 2). Thus hot spot tracks (circles) model a simulated seamount chain formed by periodic volcanic eruptions at $0.08550d/V_p$ (0.00008 diffusion time) intervals, while hot spot position markers show the intersection of the plume and the base of the plate in a fixed reference frame. (It should be noted that the periodic marking used to delineate hot spot tracks is not based on any observed physical pulsing characterized by a $0.08550d/V_p$ period.) Hot spot locations and tracks corresponding to the two distinct plumes described in the discussion above are differentiated by solid versus open rectangles and circles. The hot spot locations (rectangles) are defined by local temperature maximums in the regions surrounding each of the hot spots identified in Animation 2. The hot spot position markers and the corresponding track marker are color-coded to indicate their age. In order to demonstrate the full period of activity of each hot spot the calculation of hot spot tracks is continued regardless of whether the track marker reaches a convergent plate boundary.

[21] Both sets of hot spot locations and tracks in Figure 5 indicate that the plates are moving across the hot spots at a considerably greater velocity than the hot spot motion. The younger hot spot (solid rectangles) produces a track that is $0.75d$ (2260 km) long while migrating approximately $0.19d$ (580 km). The older and more persistent hot spot (marked with open rectangles) migrates a significant distance after a second pulse of material rises up the original plume conduit in the lower mantle and penetrates into the upper mantle some $0.25d$ (750 km) northwest (taking the positive y-direction as north) of the previous location (between diffusion times 0.000024 and 0.000032). Subsequently, the associated hot spot track grows to $2.15d$ (6440 km) in length over a period of $1.2\ d/V_p$ (0.00113 diffusion times) while the

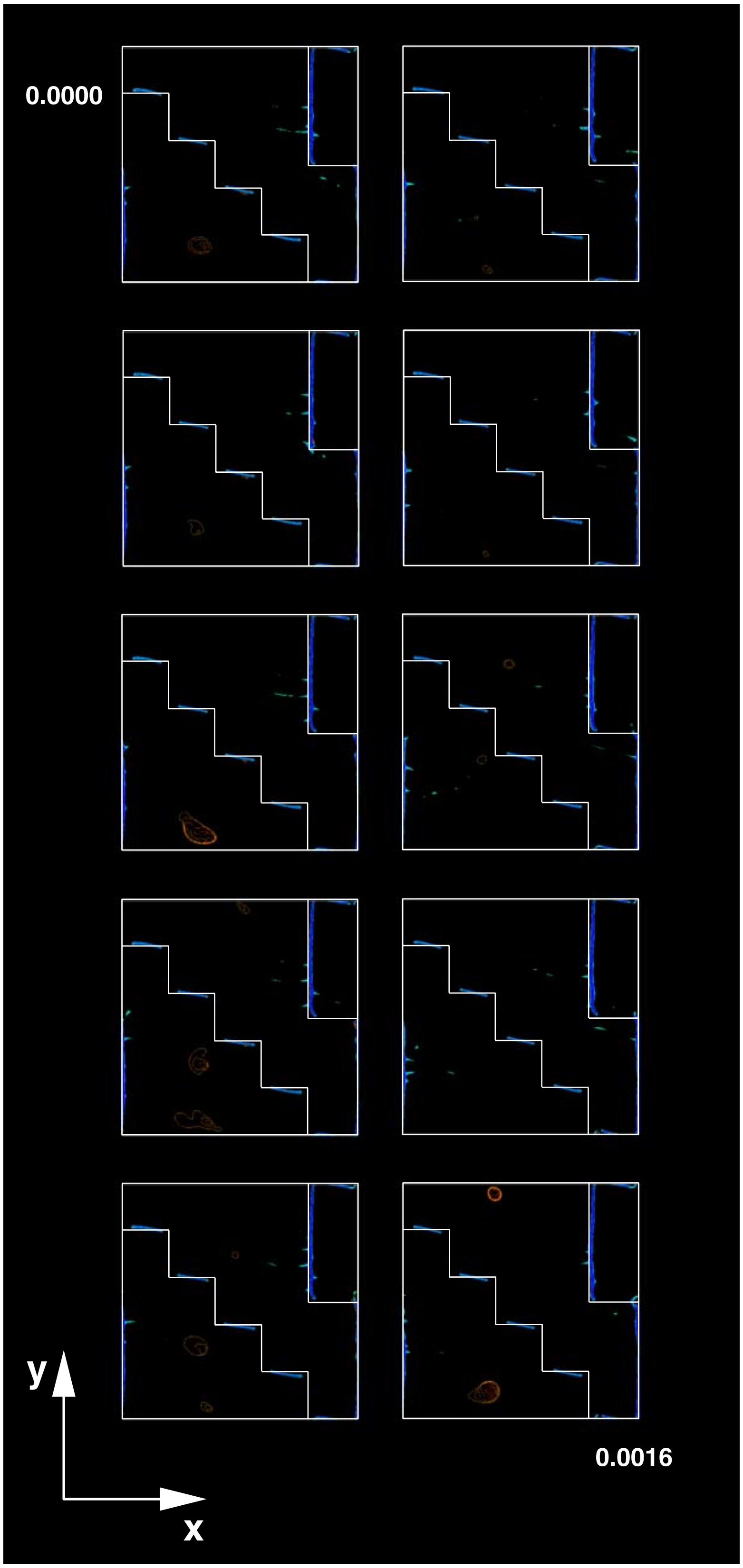

Figure 4. Temperature contour evolution at a depth of 0.083*d* (250 km) in Model 30a. The contour interval is 0.01. Contours are shown in the ranges 0.0–0.68 (blues) and 0.88–1.0 (oranges and reds).

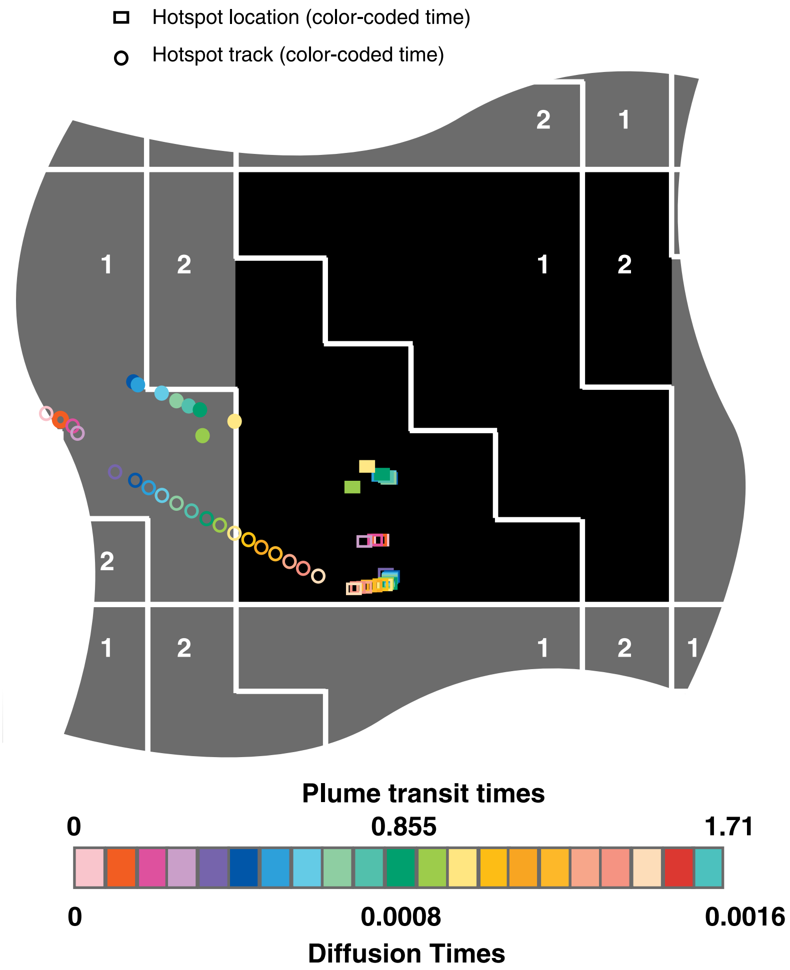

Figure 5. Map of the distribution of hot spots locations and hot spot tracks resulting from the calculation presented in Animation 1 (Model 30a) at the model surface. The map shows hot spot tracks (circles) and the position of the actual hot spots (rectangles) at 0.00008 (diffusion time) intervals during the 0.0016 time period examined. The map is drawn for a time corresponding to the final frame of Animation 1. Different colors correspond to formation time for hot spot tracks and past positions for hot spot locations. Open and filled circles and rectangles are used to distinguish between features associated with the two distinct plumes that develop below Plate 2 in Animation 1.

hot spot location migrates approximately 0.28*d* (840 km). Plume pulsing is in this case the result of developing lower thermal boundary instabilities arriving at the base of an existing upwelling [e.g., *Jarvis*, 1984; *Weinstein et al.*, 1989]. There does not appear to be any clear correlation between the direction of motion of the two plumes, nor plate and plume movement.

[22] The results obtained from Model 30a indicate that in a system with an upper mantle that is 30 times less viscous than the lower mantle, lateral plume velocities may be only a small percentage of overriding plate velocity. However, the experiment described used a plate geometry that is intended to enhance plate motion steadiness and may therefore have a similar effect on plume motion steadiness. In order to investigate this possibility we performed an alternative calculation, Model 30b, which is setup identically to Model 30a with the exception of the plate geometry.

[23] Animation 3 (see Figure 6 for still image) shows the temperature field evolution of Model 30b over a period of 1.71d/V_p (0.0016 diffusion times). The mean temperature of Model 30b is about 4% cooler than Model 30a, reflecting the fact that the smaller plates and flow reorganization events characterizing this calculation allow for a more efficient removal of heat from the system.

[24] During the period shown we concentrate on the behavior of four plumes extending from the lower thermal boundary layer to the base of the plates. One of the plumes is positioned below Plate 1 (defined in the animation), two of the plumes are located below Plate 2 and the final plume of interest appears below Plate 4.

[25] Figure 7 shows the time series of the plate velocity magnitudes from Model 30b. The time series shown corresponds to the time period depicted in Animation 3. The figure shows that the direction of motion of the two smaller plates (Plate 3 and Plate 4) changes considerably during this period. However, the direction in which Plates 1 and 2 move changes by only a small amount. The magnitude of the velocity varies considerably for all four plates.

[26] Animation 4 (see Figure 8 for still image) shows a temperature contour map on a horizontal slice through Model 30b at a depth of 0.0067*d* (200 km). The four plumes that appear in Animation 3 appear in Animation 4 as transient hot spots that undergo both periods of relatively little movement and sudden bursts of rapid migration. The longest-enduring hot spot under Plate 2 temporarily vanishes between the beginning and middle of the sequence because of the chosen contour range. However, as can be seen in Animation 3, a discernible plume conduit remains intact during the entire sequence. In Animation 4 it is clear that the temperature of the plume head cools for a period of time between pulses of hot material rising up the conduit. Comparing Animations 3 and 4 also indicates that the majority of the motion of the maturing hot spot seems to arise from shearing of the plume head, due to plate motion, rather than motion of the plume conduit.

[27] Figure 9 shows a map view at a depth of 0.0067*d* (200 km) of the history of the distribution of hot spot locations (rectangles) with associated hot spot tracks (circles) as they would appear at a time corresponding to the end of the sequence shown in Animation 3 (Model 30b). The black region represents the calculation solution domain. (Note that Plate 4 wraps around the computational domain.) Yellow and red boundaries in the figure surround corresponding hot spot locations and tracks for plumes under Plate 2 and 4 respectively. The hot spots and tracks associated with the two other plumes examined (under Plate 1 and Plate 2) are differentiated by solid versus open rectangles and circles. The position of the hot spot tracks and locations was calculated in Figure 9 using the same method described for Figure 5. The distribution of the hot spot location markers versus the length of the hot spot tracks shows that each of the plumes considered in Model 30b exhibits periods of relatively little motion when compared with plate motion.

[28] Animations 1 and 3 show that the viscosity contrast specified in Model 30a and 30b allows for the formation of vigorous intra-plate mantle plumes with lifetimes comparable to the plume-transit time (d/V_p). Moreover, the plume conduits examined in the calculations exhibit small lateral motion in comparison with the plate motion. To assess the impact of the viscosity contrast on the results presented from Models 30a and 30b we have examined two other models Model 9b and Model 90b.

[29] Animation 5 (see Figure 10 for still image) shows the evolution of the temperature field of Model 9b over a period of $1.71d/V_p$ (0.0016 diffusion times). During the sequence shown in Animation 5 three plume-like upwellings are clearly evident. The largest of these (furthest in the animation from the viewer) is positioned very close to a divergent plate boundary between Plates 1 and 4 and produces two distinct local maximums in upper mantle temperature for at least part of its life-time. The other two plumes are positioned under Plates 2 and 3. In contrast to Models 30a and 30b, the intra-plate plume-like upwellings in Model 9b are swept around in the ambient mantle flow. Moreover, fewer upwellings are present at any one time in this calculation. One upwelling that does appear for a long period is caught below the divergent Plate 1 and Plate 4 boundary and the upwelling flow associated with the plume appears to be strongly coupled to the plate scale flow. Indeed, a number of minor upwelling features in this calculation appear to form in the regions below divergent plates boundaries. Moreover, the shape

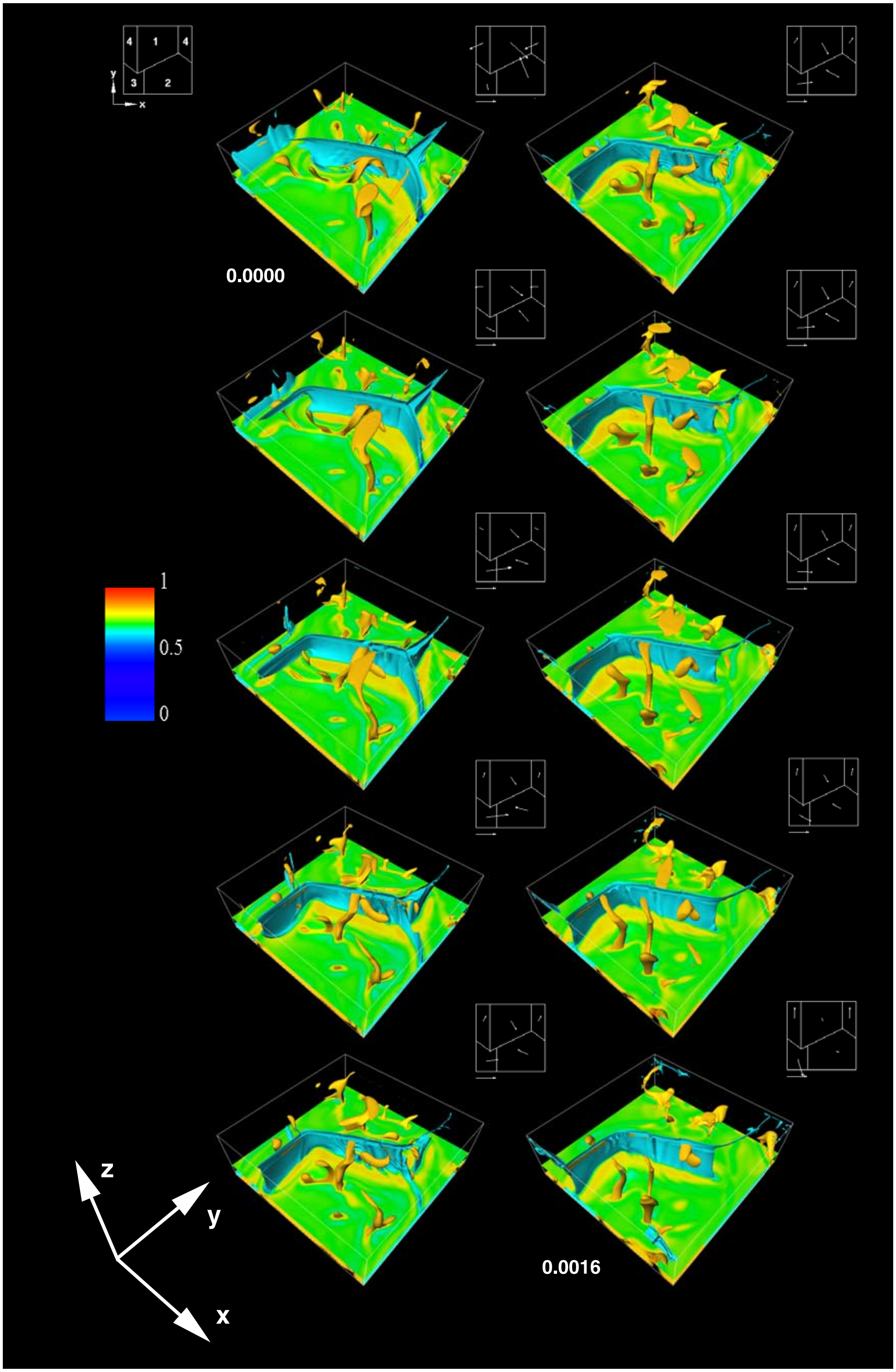
4
1
4
3
2
y
x
0.0000
1
0.5
0
z
y
x
0.0016

of the upwellings in Model 9b do not generally appear as features with disk shaped heads and attached conduits. This observation should be expected when the hot upwellings in the model are controlled by the plate scale motion driving a passive hot return flow rather than hot material independently breaking away from a lower thermal boundary layer.

[30] Figure 11 shows the time series of the plate velocity magnitudes from Model 9b. The time series shown corresponds to the period depicted in Animation 5. The direction of plate motion of each of the four plates in this model is extremely steady. It is apparent that the greater degree of lateral plume motion in Model 9b does not appear to be due to a greater variation in plate motion in this calculation. We therefore conclude that the transient nature of the plumes in Model 9b is due to the smaller viscosity contrast between the upper and lower mantle.

[31] Animation 6 (see Figure 12 for still image) shows a temperature contour map on a horizontal slice through Model 9b at a depth of $0.083d$ (250 km). Each of the three upwellings described above appears as a distinct hot spot in the sequence. This animation also reveals the interesting double-headed nature of the large upwelling seen in Animation 5. Although one head of this hot spot feature remains rather stationary (near a divergent plate boundary), the other hot spot associated with the largest upwelling drifts rapidly during its lifetime, as do the two other hot spots in the animation which show considerable motion during their brief periods of existence.

[32] Figure 13 shows a map view at a depth of $0.083d$ (250 km) of the history of the distribution of hot spot locations (rectangles) and associated hot spot tracks (circles) as they would appear at a time corresponding to the end of the sequence shown in Animation 5 (Model 9b). Hot spot locations and tracks are determined as described in the discussion of Figures 5 and 9. Yellow and red boundaries surround corresponding hot spot locations and tracks for the two intra-plate hot spots. The two local hot spots associated with the largest and longest prevailing upwelling near the Plate 1 and Plate 4 divergent boundary are distinguished using open and filled markers. Comparing the length of the hot spot track to the distance covered by the hot spot during the corresponding interval indicates that with the exception of the hot spot caught at the divergent plate boundary, the hot spots in Model 9b migrate with a speed comparable to the overriding plate velocity.

[33] Animation 7 (see Figure 14 for still image) shows the temperature field evolution of Model 90b over a period of $1.71d/V_p$ (0.0016 diffusion times). During the period shown, we have concentrated on analyzing the behavior of five dominant plume-like upwellings that extend from the lower thermal boundary layer to the base of the plates. However, there are other upwellings that either appear briefly or eventually merge or coalesce with the features we focus on in the description below. The first

Figure 6. Temperature field evolution in Model 30b. The calculation has periodic (wrap-around) boundary conditions and incorporates four plates with thicknesses of $0.052d$ (150 km). The Rayleigh numbers specified for the calculation (based on the lower mantle viscosity) are $Ra_B = 1.666 \times 10^6$ and $Ra_H = 2.5 \times 10^7$. Viscosity decreases by a factor of 30 above a depth of $0.22d$ (670 km). The blue isosurface has a temperature of 0.65 and the orange isosurface has a temperature of 0.85. The blue isosurface is cropped at a depth of $0.069d$ (200 km). The color legend indicates the colour palette used in the figure. The co-ordinate axes to the lower left indicate the orientation of the depicted temperature field relative to other figures and animations from Model 30b. The surface plate geometry is indicated at the upper left with a numerical referencing system. Plate velocity is also shown to the upper right of each corresponding temperatue field with arrows superimposed on a planview of the plate geometry to indicate the instantaneous direction of plate motion above the temperature field. Arrow lengths are time-dependent and are proportional to a plate velocity magnitude of 1000d/diffusion-time, which is indicated by the length of the arrow below each plate velocity panel. The first and final panels in the sequence are indicated by start time and end time labels of 0.0000 and 0.0016 diffusion times, respectively. Panels are shown at intervals of approximately 0.000178 diffusion times. Calculations were performed on a 16 processor Beowulf cluster and required approximately 1 Gigabyte of RAM per process. Each calculation is computed on a $325 \times 325 \times 129$ node grid and models a volume with physical dimensions of $3 \times 3 \times 1$.

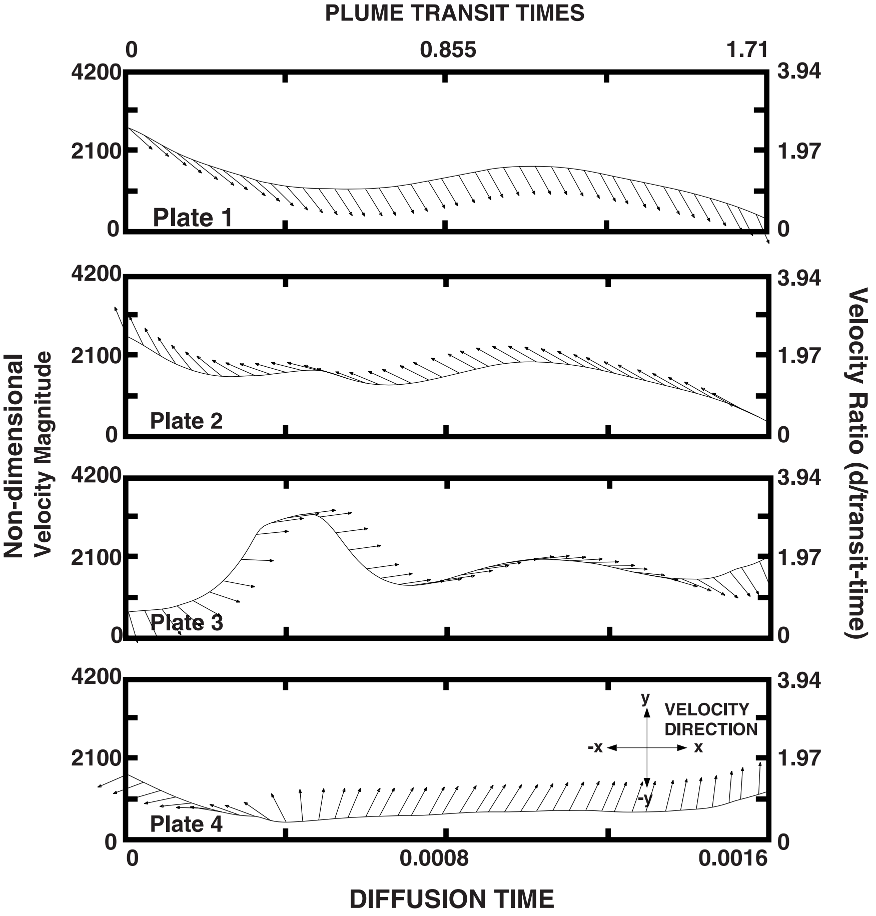

Figure 7. Plate velocity time series for Model 30b. Plate velocity magnitude is shown in accord with the plate numbering system introduced in Figure 1. Arrows are attached to the velocity magnitude curves at an interval of 0.00004 (diffusion time) and show the direction of the plate motion at the corresponding instant. The time series corresponds to the period shown in Animation 3.

plume of interest is centrally positioned under Plate 3 and slowly grows throughout the sequence shown. A second plume forms and subsequently merges with another large plume under Plate 1. The other three upwellings of interest are all located below Plate 2 and are particularly complex. One of these hot spots is associated with a slowly dissipating plume that is clearly visible near the beginning of the sequence presented in Animation 7 but is more clearly revealed in Animation 8 (see Figure 15 for still image). The other two hot upper mantle features below Plate 2 are different upper mantle branches of the same lower mantle conduit. This upwelling (closest to the viewer in Animation 7) pulses with surges of hot material traveling up a fairly stationary lower mantle conduit. The pulses originate with the arrival of developing plumes arriving at the base of the mature plume and lead to the formation of complex structures characterized by two plume heads branching off of the same conduit. These plume heads overlap temporally but not spatially (as each originates with the arrival of a different developing thermal boundary layer instability at the site of the upwelling flow) and thus produce distinct neighboring hot spots supplied by the same lower mantle source.

[34] In contrast to Model 9b, the upwellings in Model 90b form into plume-like features, characterized by distinct persisting thermal plume conduits and disk-shaped heads that extend outward below the base of the plates. Also in contrast to the upwellings in Model 9b, lower mantle upwellings

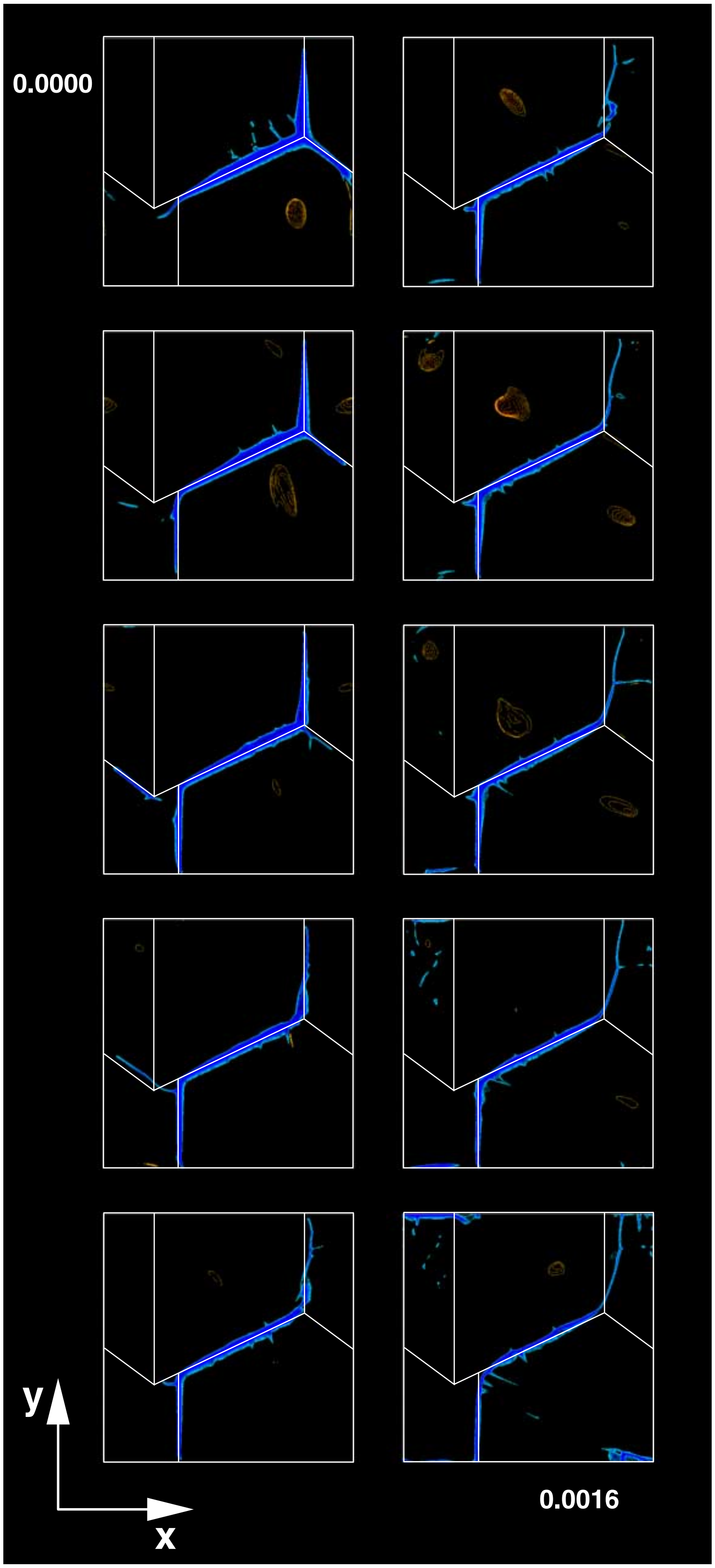

Figure 8. Temperature contour evolution at a depth of 0.067*d* (200 km) in Model 30b. The contour interval is 0.01. Contours are shown in the ranges 0.0–0.65 (blues) and 0.85–1.0 (oranges and reds).

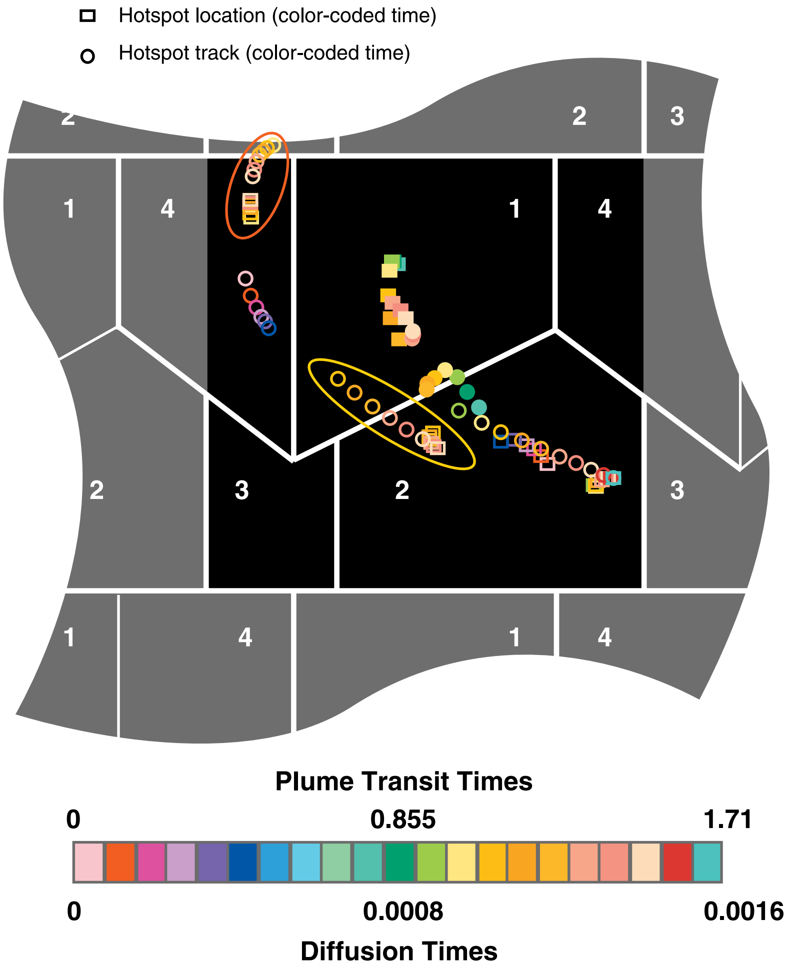

Figure 9. Map of the distribution of hot spot locations and hot spot tracks resulting from the calculation presented in Animation 3 (Model 30b) at the model surface. The map shows hot spot tracks (circles) and the position of the actual hot spots (rectangles) at 0.00008 (diffusion time) intervals during the 0.0016 time period examined. The map is drawn for a time corresponding to the final frame of Animation 3. Different colors correspond to formation time for hot spot tracks and past positions for hot spot locations. Filled and open circles and rectangles are used to distinguish between features associated with the two distinct plumes that develop below Plates 1 and 2, respectively. Two other distinct sets of associated hot spot location markers and tracks are enclosed by a pair of red and yellow oval boundaries.

remain relatively fixed compared with plate motion and do not appear to have any correlation with the position of divergent plates. The greatest degree of lateral plume conduit motion seems to occur when neighboring plumes coalesce, rather than being coupled to plate motion.

[35] Figure 16 shows the time series of the plate velocity magnitudes from Model 90b. The time series shown is for the $1.71 d/V_p$ (0.0016 diffusion time) period depicted in Animation 7. The figure shows that the two larger plates (1 and 2) move in a fairly constant direction for almost the entire period examined. In contrast, Plate 3 changes direction quite gradually over most of the first half of the examined period. The total change in direction is roughly 60 degrees. Plate 4 shows two rather rapid changes in direction (starting at approximately 0.0008 and 0.0014 diffusion times). All of the plates show highly variable velocity magnitude. The onset of subduction between Plates 3 and 4 is marked by a rapid rise in the velocity of these

plates starting at about $0.855d/V_p$ (0.0008 diffusion times).

[36] Animation 8 shows contours of the temperature field at a depth of $0.067d$ (200 km) in Model 90b. At this depth, plume heads associated with the upwellings in Animation 7 appear as massive yellow and red circular regions over a thousand kilometers in diameter. (As in similar previous figures, cold downwelling sheets associated with slabs appear as linear blue features.) Within each of these regions it is generally the case that a focussed hot anomaly of no more than $0.033d$–$0.067d$ (100–200 km) across is visible. It is the motion of this hot local maximum in temperature that we track as the plume-related hot spot.

[37] The most striking feature of Animation 8 is that plume heads are almost stationary during their existence. Although we observe that plume head shape is often sheared by plate movement, hot spot motion (determined by the motion of the hottest part of the plume head) is only a small percentage of plate motion ($\sim$10%).

[38] Figure 17 presents a map view at a depth of $0.067d$ (200 km) of the history of the distribution of hot spot locations (rectangles) and associated hot spot tracks (circles) for Model 90b. Yellow, red and blue boundaries are used to isolate corresponding hot spots and tracks associated with three distinct upwellings. Different plume heads associated with a single plume conduit below Plate 2 (described above) are differentiated by open and closed markers. Due to the variation in plate velocities, hot spot tracks vary in length from $1.0d$ (3000 km) to over $3.0d$ (9000 km). The plume conduits typically prevail for periods ranging from $0.68d/V_p$ to $1.62d/V_p$ (0.00064 to 0.00152 diffusion times). As can be seen by the clustering of the majority of the rectangular hot spot location markers, hot spots move by only a fraction of the hot spot track lengths during these periods.

[39] The hot spot on Plate 3 is produced by a large plume that develops below that plate (Animation 7). Initially this hot spot is migrating quite rapidly in the direction of the emerging convergent plate boundary. However, as cold material associated with the plate material subducted between Plates 3 and 4 plunges into the lower mantle, the plume is swept away from its initial location and the hot spot actually passes back over its original location $0.51d/V_p$ (0.00048 diffusion times) after it first appears, having travelled a total round-trip distance of nearly $0.7d$ during its existence. The initial migration of the hot spot toward the emerging convergent plate boundary is due to the large velocities in the upper mantle resulting from the rapid motion of the plate toward the young subduction zone. Behavior characterized by hot spots initially migrating toward young subduction zones, returning to their original position, and then eventually moving away from the convergent boundary was observed in several other calculations not included in this presentation.

4. Discussion and Conclusions

[40] Our findings indicate that the formation of active, focussed, columnar upwellings is prevalent in three-dimensional numerical mantle convection models incorporating plate-like surface motion, a significant degree of internal heating and a stratified viscosity that increases with depth by a factor of 30 or 90. The morphology of the upwelling features is generally plume-like and evolves into structures with clearly defined conduits and heads as the contrast between lower and upper mantle viscosity is increased. In all of the calculations, downwelling flow is focussed in cold sheet-like features supplied by a flux of cold plate material into the mantle along linear convergent plate boundaries. The sheet-like downwellings in our calculations simulate the subduction of slabs of oceanic lithosphere.

[41] The longevity of the 15 hot spots included in Figures 5, 9, 13, and 17 is summarized in Figure 18. Plume lifetime variability is indicated as a function of overriding plate velocity and the ratio of lower mantle to upper mantle viscosity (viscosity ratio). Hot spot longevity is based on the total period of time that each hot spot continued to generate a hot spot track in each of the four map figures (Figures 5, 9, 13, and 17). Hot spots with a lifetime of less than 0.5 plume-transit times are indicated by a square symbol. Hot spots repre-

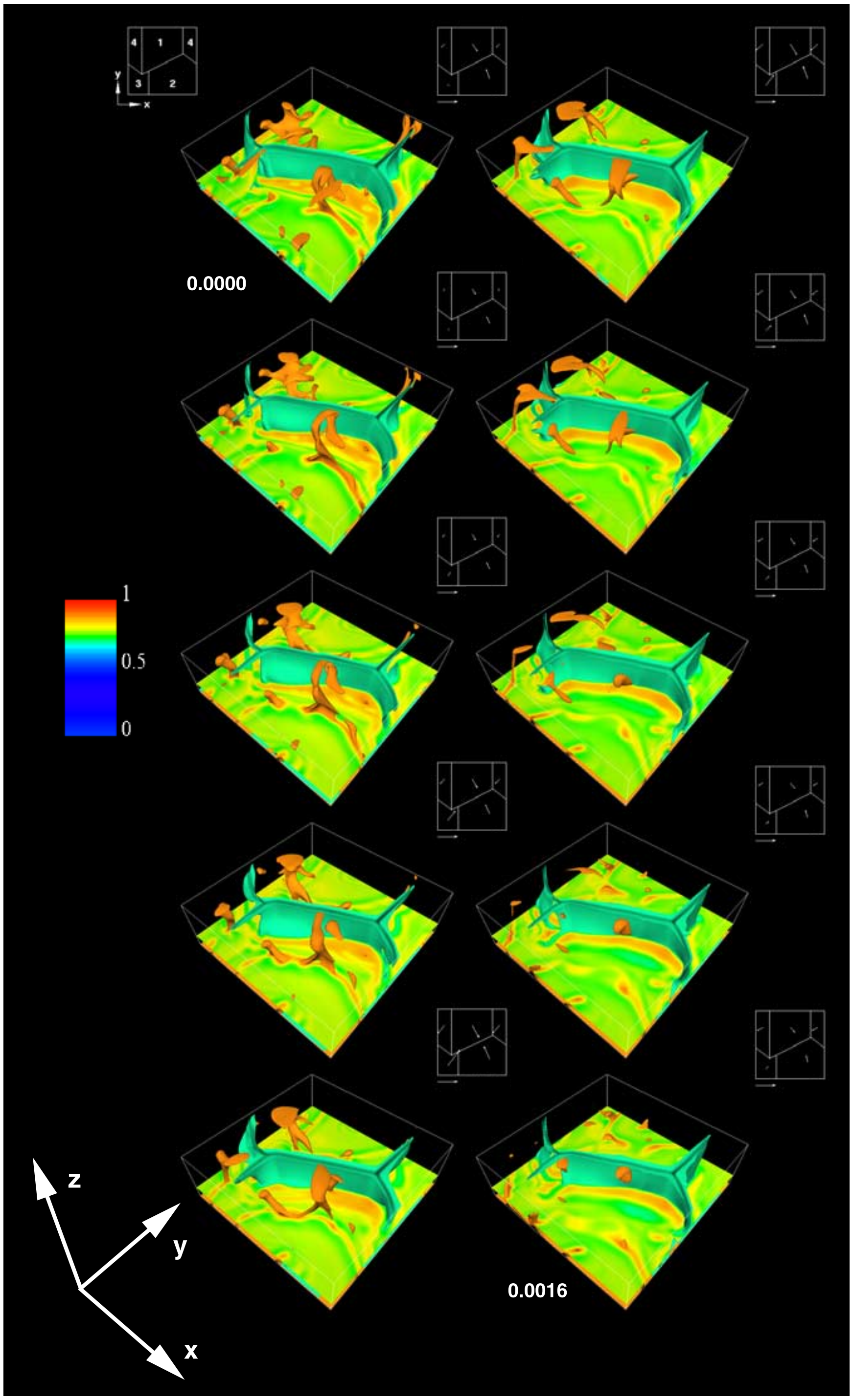
4
1
4
3
2
y
x
0.0000
1
0.5
0
z
y
x
0.0016

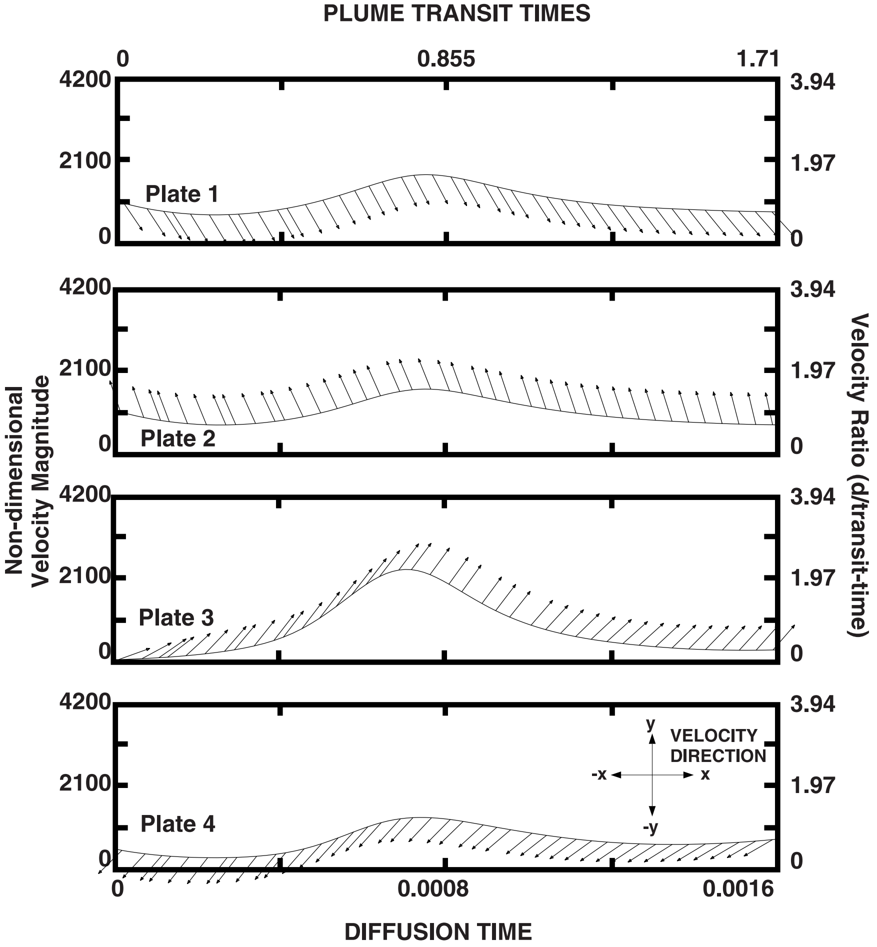

Figure 11. Plate velocity time series for Model 9b. Plate velocity magnitude is shown in accord with the plate numbering system introduced in Figure 1. Arrows are attached to the velocity magnitude curves at an interval of 0.00004 (diffusion time) and show the direction of the plate motion at the corresponding instant. The time series corresponds to the period shown in Animation 5.

Figure 10. Temperature field evolution in Model 9b. The calculation has periodic (wrap-around) boundary conditions and incorporates four plates with thicknesses of 0.052*d* (150 km). The Rayleigh numbers specified for the calculation (based on the lower mantle viscosity) are $Ra_B = 1.666 \times 10^6$ and $Ra_H = 2.5 \times 10^7$. Viscosity decreases by a factor of 9 above a depth of 0.22*d* (670 km). The greenish-blue isosurface has a temperature of 0.69 and the orange isosurface has a temperature of 0.89. The blue isosurface is cropped at a depth of 0.069*d* (200 km). The color legend indicates the colour palette used in the figure. The co-ordinate axes to the lower left indicate the orientation of the depicted temperature field relative to other figures and animations from Model 9b. The surface plate geometry is indicated at the upper left with a numerical referencing system. Plate velocity is also shown to the upper right of each corresponding temperature field with arrows superimposed on a planview of the plate geometry to indicate the instantaneous direction of plate motion above the temperature field. Arrow lengths are time-dependent and are proportional to a plate velocity magnitude of 1000d/diffusion-time, which is indicated by the length of the arrow below each plate velocity panel. The first and final panels in the sequence are indicated by start time and end time labels of 0.0000 and 0.0016 diffusion times, respectively. Panels are shown at intervals of approximately 0.000178 diffusion times. Calculations were performed on a 16 processor Beowulf cluster and require approximately 1 Gigabyte of RAM per process. Each calculation is computed on a 325 × 325 × 129 node grid and models a volume with physical dimensions of 3 × 3 × 1.

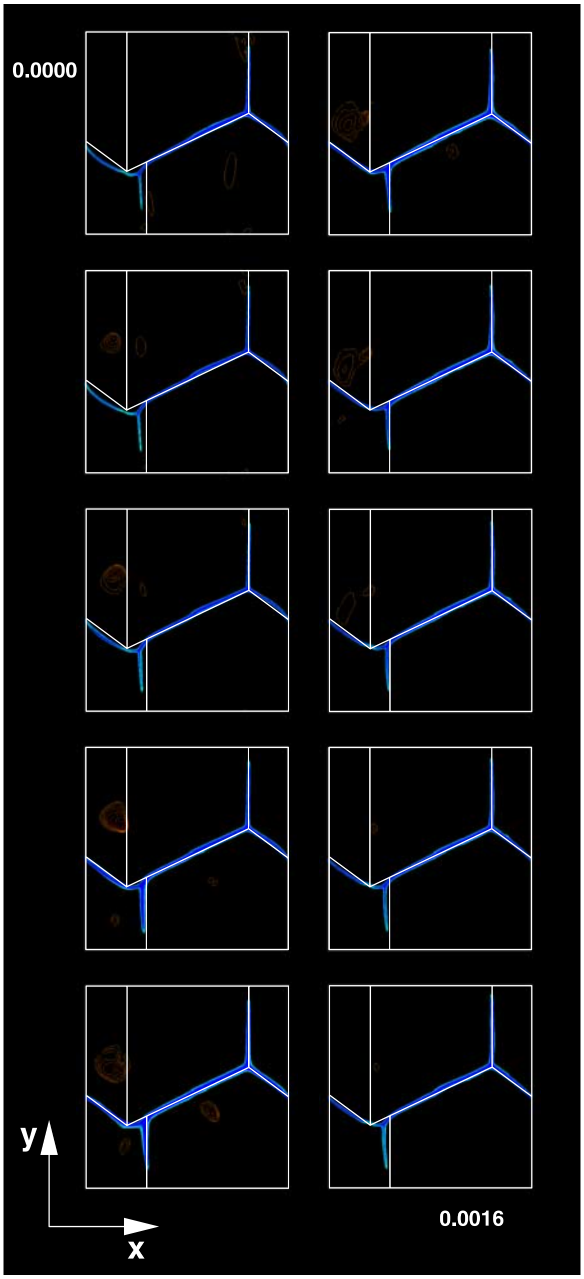

Figure 12. Temperature contour evolution at a depth of 0.083*d* (250 km) in Model 9b. The contour interval is 0.01. Contours are shown in the ranges 0.0–0.69 (blues) and 0.89–1.0 (oranges and reds).

sented by other symbols indicate longer-lived hot spots. Colors and open versus closed symbols conform to the system used to distinguish the hot spots in the corresponding map figures (see figure caption for detail). Overriding plate velocity is determined by calculating the average plate velocity during the period corresponding to the lifetime of the hot spot.

[42] The shortest lived hot spots that we observe appear in Model 9b. Intra-plate hot spots in this calculation were also the most mobile, generally migrating over distances comparable to the length of the hot spot tracks they produce (see Figure 13). This model also included an upwelling situated below a region of plate divergence which persisted as a nearly stationary hot spot for a period slightly greater than a plume-transit time.

[43] In Models 30a and 30b hot spots generally persist for periods in excess of $0.5d/V_p$. Only one exception appears in Figure 18. In Model 30a we also find that the plume locations are quite stationary, despite the overriding plate velocity exceeding the estimated plume-transit velocity, V_p. Thus we find stationary plumes in the parameter space where plume motion was observed to be strongly controlled by plate scale motion in temperature-dependent viscosity fluids that do not include any viscosity depth dependence [e.g., *Jellinek et al.*, 2003]. In Model 30a we find that the location of the longest lived hot spot is confined to a circle of radius 0.17*d* (500 km) over a period of $1.1d/V_p$, while it produces a hot spot track on the overriding plate that is over 1.58*d* (4750 km) long. The mean velocity of the nearly steady plate motion is eleven times greater than the hot spot migration rate over the first $0.51d/V_p$ of the hot spot's existence although this ratio decreases to a factor of three as the hot spot ages. Model 30b also exhibits several examples of plumes that endure in nearly fixed locations for periods ranging from $0.57d/V_p$ to $0.86d/V_p$. Model 90b shows a variety of plume behavior including a number of intra-plate nearly stationary plumes (Animation 7). In this model, hot spot velocities are less than 10% of plate velocities for plumes below plates moving at $0.8V_p$ to $1.7V_p$, but as great as 35% of the plate velocity for a hot spot below a plate moving at approximately $2.7V_p$.

[44] Model 90b features the most vigorous, well-formed plumes, with hot upwellings displaying broad heads fed by well-defined, columnar conduits. In contrast, Model 9b features fewer plumes

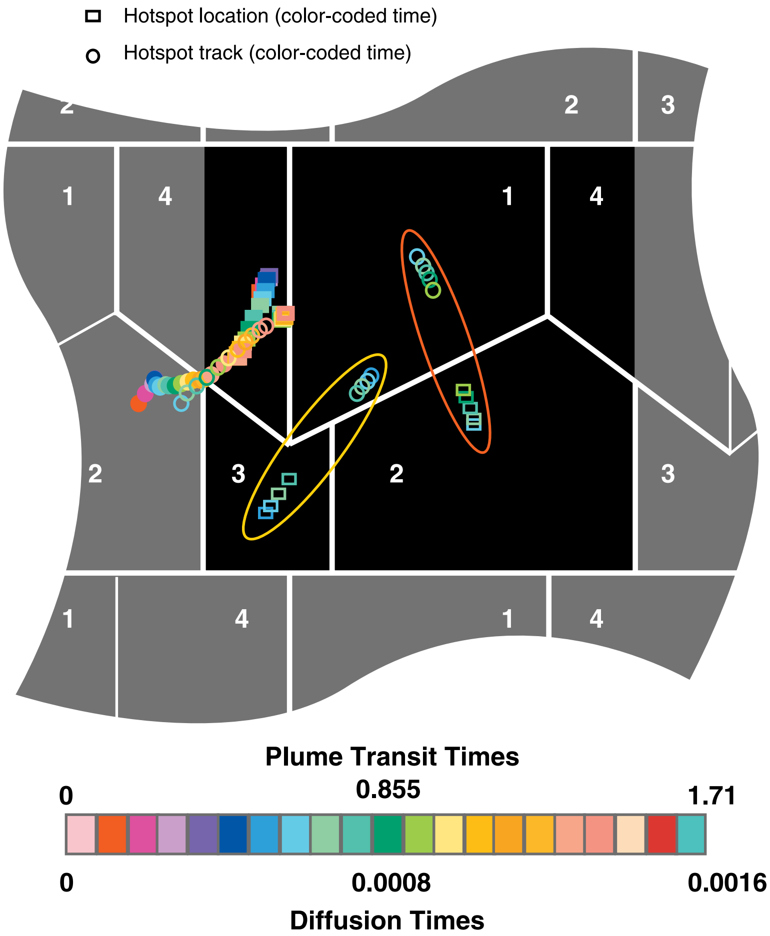

Figure 13. Map of the distribution of hot spot locations and hot spot tracks resulting from the calculation presented in Animation 5 (Model 9b) at the model surface. The map shows hot spot tracks (circles) and the position of the actual hot spots (rectangles) at 0.00008 (diffusion times) intervals during the 0.0016 time period examined. The map is drawn for a time corresponding to the final frame of Animation 1. Different colors correspond to formation time for hot spot tracks and past positions for hot spot locations. Filled and open circles and rectangles are used to distinguish between features associated with the two distinct plumes that develop below Plate 4 in Animation 5. Two other distinct sets of associated hot spot location markers and tracks are enclosed by a pair of red and yellow oval boundaries.

than other calculations and a greater propensity for plumes to form close to divergent plate boundaries. This behavior indicates that plume positioning and formation is at least partly affected by the influence of plate-scale flow if the upper and lower mantle viscosities vary by no more than an order of magnitude [e.g., *Jellinek et al.*, 2003]. The increase in the ratio of lower mantle to upper mantle viscosity effectively allows for the concentration of higher horizontal velocities throughout the relatively weak upper mantle and these strongly align with plate motion. However, as the viscosity stratification is increased, the depth to which high horizontal mantle velocities align with plate motion and penetrate into the lower mantle diminishes. Instead, throughout most of the lower mantle, sluggish, plate-scale return flow is directed oppositely to the motion of the overriding plate and locally the velocity field is dominated by the buoyancy of active plumes. Consequently, plume conduits in the lower mantle of Model 90b are less influenced by plate motion

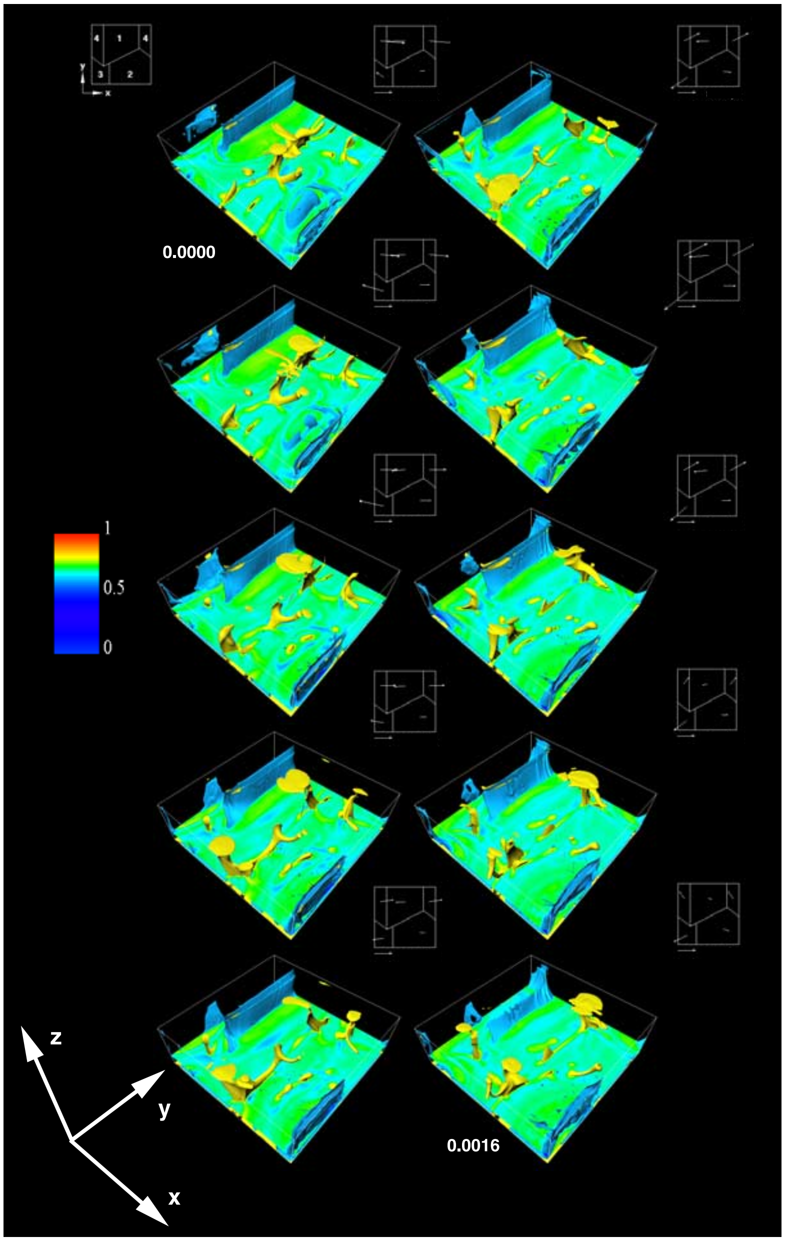

Figure 14. Temperature field evolution in Model 90b. The calculation has periodic (wrap-around) boundary conditions and incorporates two plates with thicknesses of 0.052*d* (150 km). The Rayleigh numbers specified for the calculation (based on the lower mantle viscosity) are $Ra_B = 1.666 \times 10^6$ and $Ra_H = 2.5 \times 10^7$. Viscosity decreases by a factor of 90 above a depth of 0.22*d* (670 km). The blue isosurface has a temperature of 0.61 and the yellow isosurface has a temperature of 0.81. The blue isosurface is cropped at a depth of 0.069*d* (200 km). The color legend indicates the colour palette used in the animation. The co-ordinate axes to the lower left indicate the orientation of the depicted temperature field relative to other f igures and animations from Model 90b. The surface plate geometry is indicated at the upper left with a numerical referencing system. Plate velocity is also shown to the upper right of each corresponding temperature field by using arrows superimposed on a planview of the plate geometry to indicate the instantaneous direction of plate motion above the temperature field. Arrow lengths are time-dependent and are proportional to a plate velocity magnitude of 1000d/diffusion-time, which is indicated by the length of the arrow below each plate velocity panel. The first and final panels in the sequence are indicated by start time and end time labels of 0.0000 and 0.0016 diffusion times, repectively. Panels are shown at intervals of approximately 0.000178 diffusion times. Calculations were performed on a 16 processor Beowulf cluster and required approximately 1 Gigabyte of RAM per process. Each calculation is computed on a 325 × 325 × 129 node grid and models a volume with physical dimensions of 3×3×1.

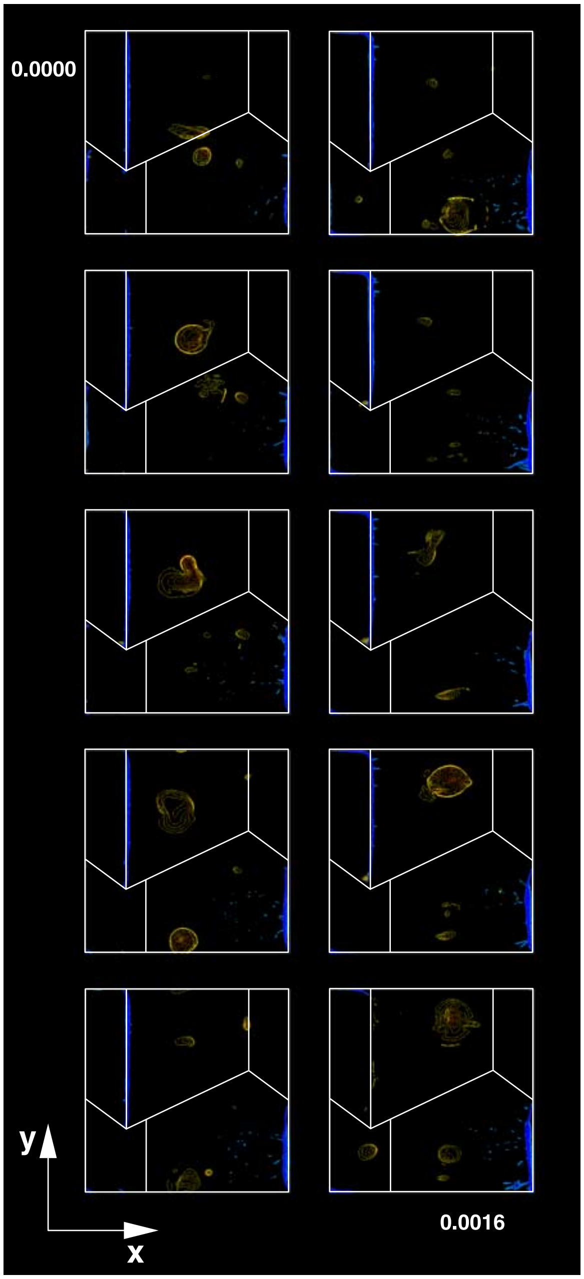

Figure 15. Temperature contour evolution at a depth of 0.067d (200 km) in Model 90b. The contour interval is 0.01. Contours are shown in the ranges 0.0–0.61 (blues) and 0.81–1.0 (yellows, oranges and reds).

and their positions become almost fixed when the upper mantle-lower mantle viscosity contrast is increased.

[45] The value of the ratio of the dynamic viscosity of the cold fluid above the thermal boundary layer to the fluid in contact with the hot boundary, λ, is equal to 1 in each of our calculations. In a recent study, *Jellinek et al.* [2003] studied flow in a model with a rigid bottom boundary and found λ affected the relative scaling of the velocity and thermal boundary layers. Consequently, the value of λ affected plume formation and spacing and the ability of large-scale plate motion to advect plumes. In a model with a free-slip basal boundary condition, such as ours, analogous velocity boundary layers do not develop. Nevertheless, it is possible that our results may differ for different values of λ. Further calculations including temperature-dependent viscosity should be the subject of a future study.

[46] In a study of plume advection in large-scale flow in the mantle driven entirely by surface plate motion and the negative buoyancy of lower mantle density heterogeneities, *Steinberger and O'Connell* [1998] found that slow relative motion of plume associated hot spots required an upper mantle viscosity that is on average about two orders of magnitude less than the viscosity of the lower mantle. Our findings also indicate that a viscosity increase of this magnitude produces very slow moving persistent hot spots, associated with well-developed plumes. However, we also find examples of persistent (lifetimes $>0.5d/V_p$), almost spatially fixed, hot spots in calculations with upper mantle-lower mantle viscosity contrasts as low as 30. The fact that we find examples of stationary plumes with such a viscosity model most likely results from the tendency for plumes to form, or be swept into, stagnation points in our fully dynamic calculations. In comparison, *Steinberger and O'Connell* [1998] placed plumes where they would match actual hot spot locations. Consequently, plumes in their calculations did not generally originate from flow stagnation points. This point was discussed previously by *Zhong et al.* [2000], who examined plume motion in a spherical geometry calculation with a lower mantle to upper mantle viscosity ratio of 60 and concluded that the horizontal motion in the vicinity of upwellings is, to first order, influenced by mantle flow determined by slab buoyancy (i.e., the

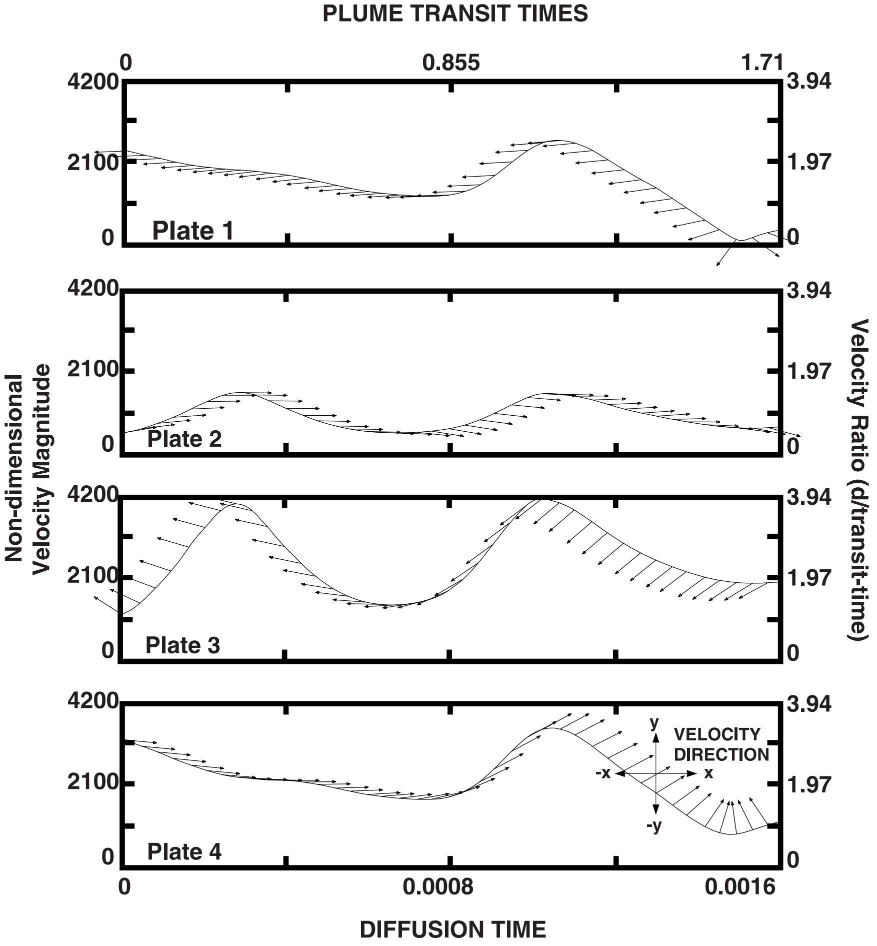

Figure 16. Plate velocity time series for Model 90b. Plate velocity magnitude is shown in accord with the plate numbering system introduced in Figure 1. Arrows are attached to the velocity magnitude curves at an interval of 0.00004 (diffusion times) and show the direction of the plate motion at the corresponding instant. The time series corresponds to the period shown in Animation 7.

plate-scale convection pattern). However, *Zhong et al.* [2000] also report observing persistent stationary plumes under fast moving plates, as we do, and note that localized plume buoyancy, combined with a high viscosity lower mantle, may play an important role in determining mantle plume stationarity.

[47] A number of the plumes in this study appear to intermittently increase in buoyancy. This pulsing behavior is largely the result of immature lower thermal boundary layer instabilities being swept into flow stagnation points where they add to the buoyancy of a fixed upwelling feature [*Jarvis*, 1984; *Weinstein et al.*, 1989]. The periodicity of this type of pulsing is determined by the time-scale for the growth of thermal boundary layer instabilities at the base of the system in comparison to plume rise-time. Pulsing originating at the viscosity interface does not occur in these calculations. *Van Keken and Gable* [1995] also noted previously that the pulsating diapiric flows that evolve at viscosity interfaces in 2-D models [*Van Keken et al.*, 1992] are not evident in comparable 3-D Newtonian systems, in agreement with our observations.

[48] Clearly our model differs from the Earth because it does not allow for plate boundary migration. Furthermore the physical dimensions of our calculations are limiting as each of the plates in the model is relatively small compared to the dimensions of the Earth's largest plates. We argue that in fact it is the size restriction on the

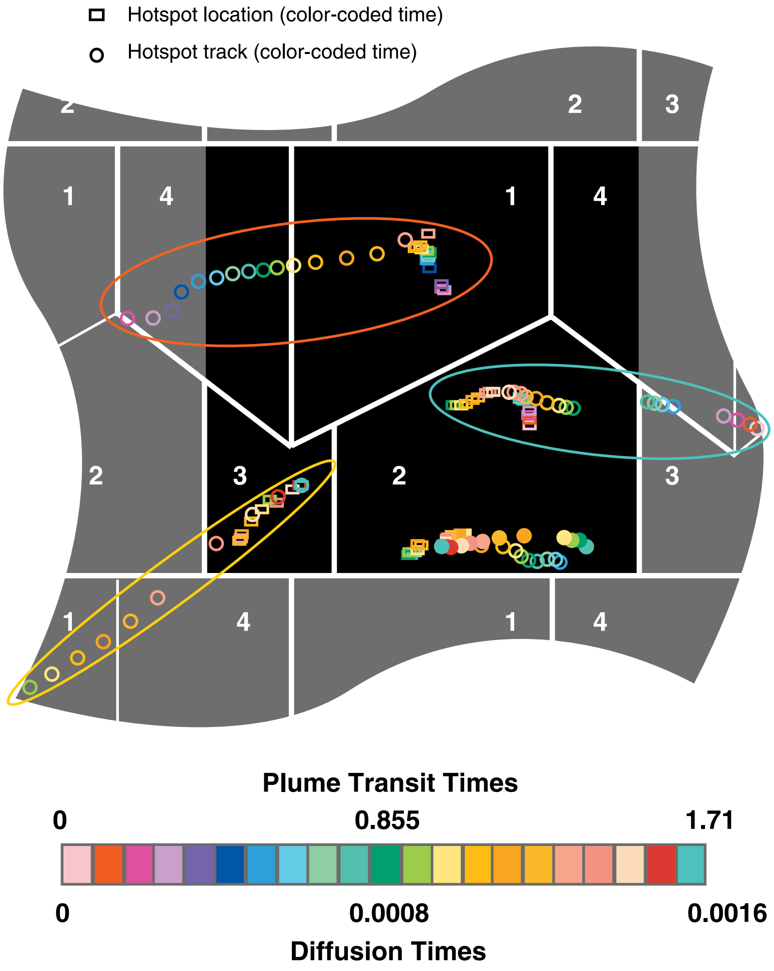

Figure 17. Map of the distribution of hot spot locations and hot spot tracks resulting from the calculation presented in Animation 7 (Model 90b) at the model surface. The map shows hot spot tracks (circles) and the position of the actual hot spots (rectangles) at 0.00008 (diffusion time) intervals during the 0.0016 time period examined. The map is drawn for a time corresponding to the final frame of Animation 1. Different colors correspond to formation time for hot spot tracks and past positions for hot spot locations. Filled and open circles and rectangles are used to distinguish between features associated with the two distinct plumes that develop below Plate 2 in Animation 7. Three other distinct sets of associated hot spot location markers and tracks are enclosed by blue, red and yellow oval boundaries.

calculations that justifies a study without evolving plate boundaries. Many hot spots below the Earth's largest plates are positioned thousands of kilometers away from the nearest plate boundary. In order to distill the effect of mantle viscosity stratification on plume associated hot spot stability in regions isolated from the influence of plate boundaries it is appropriate to keep the regions below the plates isolated from the effects of plate boundary evolution. Whether plate boundary motion and a larger model would significantly affect our findings should be the subject of a future study.

[49] Although there does not appear to be a steadfast rule to describe plume motion in this limited number of highly time-dependent calculations, with the exception of Model 9b, we find a number of examples of well-formed approximately stationary plumes in each calculation. The dynamic behavior of the plumes from our findings also fits with observations that not every plume is relatively

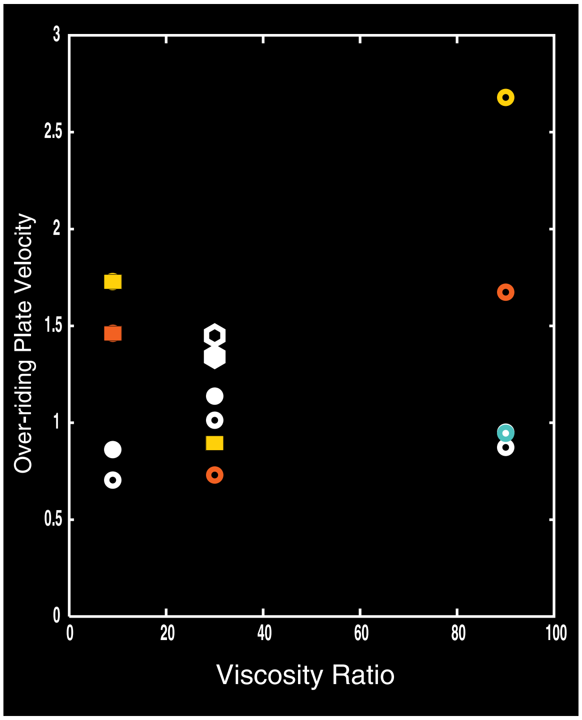

Figure 18. Plume longevity as a function of the time-averaged plate velocity of the overriding plate and the ratio of the lower mantle to upper mantle viscosity. Squares indicate plume-related hot spots that appear for less than $0.5d/V_p$ (plume-transit times). Hexagons and circles indicate plume-related hot spots that appear for more than $0.5d/V_p$ in calculations with the plate geometries shown in Figures 1a and 1b, respectively. Colors correspond to the designation system already introduced in Figures 5, 9, 13, and 17. That is, blue, yellow and red symbols correspond to hot spots that were enclosed by an oval of the same color in the earlier figures. Open and closed white symbols correspond to remaining hot spots in the earlier figures that were distinguished by either open or closed markers. Over-riding plate velocity is determined by calculating the average plate velocity during the lifetime of each hot spot.

stationary. Like the plume-related hot spots in our calculations, many real hot spots are variable, producing either segmented tracks or short pulses of activity [*Schubert et al.*, 2001]. This complete range of behavior is displayed in our Models 30b and 90b.

Acknowledgments

[50] Many thanks to Stuart Borthwick for writing the scripts to animate our results. This manuscript was improved considerably thanks to an insightful review by Mark Jellinek. Peter van Keken and Bernhard Steinberger contributed additional reviews. JPL is funded by NERC grant NER/M/S/2001/00092. SDK is funded by EAR-0207222 from the National Science Foundation. This work was partially supported by the Institute for Geophysics and Planetary Physics and EES Division at Los Alamos National Laboratory.

References

Bercovici, D. (2003), The generation of plate tectonics from mantle convection, *Earth. Planet. Sci. Lett.*, *205*, 107–121.

Brunet, D., and D. A. Yuen (2000), Mantle plumes pinched in the transition zone, *Earth Planet. Sci. Lett.*, *178*, 13–27.

Buffet, B. A., H. E. Huppert, J. R. Lister, and A. W. Woods (1992), Analytical model for solidification of the Earth's core, *Nature*, *356*, 329–331.

Bunge, H.-P., M. A. Richards, and J. R. Baumgardner (1997), A sensitivity study of three-dimensional spherical mantle convection at 108 Rayleigh number: Effects of depth-dependent viscosity, heating mode, and an endothermic phase change, *J. Geophys. Res.*, *102*, 11,991–12,007.

Chandrasekhar, S. (1961), *Hydrodynamic and Hydromagnetic Stability*, *Int. Ser. Monogr. Phys.*, 654 pp., Oxford Univ. Press, New York.

Chase, C. G. (1979), Subduction, the geoid, and lower mantle convection, *Nature*, *282*, 464–468.

Davaille, A. (1999), Simultaneous generation of hotspots and superswells by convection in a heterogeneous planetary mantle, *Nature*, *402*, 756–760.

Davaille, A., G. Girard, and M. Le Bars (2002), How to anchor hotspots in a convecting mantle?, *Earth Planet Sci. Lett.*, *203*, 621–634.

Davies, G. F. (1989), Mantle convection with a dynamic plate: Topography, heat flow and gravity anomalies, *Geophys. J.*, *98*, 461–464.

Duncan, R. A. (1981), Hotspots in the southern oceans: An absolute frame of reference for motion of the Gondwana continents, *Tectonophysics*, *74*, 29–42.

Feighner, M. A., and M. A. Richards (1995), The fluid dynamics of plume-ridge and plume-plate interactions: An experimental investigation, *Earth Planet. Sci. Lett.*, *129*, 171–182.

Gable, C. W., R. J. O'Connell, and B. J. Travis (1991), Convection in three dimensions with surface plates: Generation of toroidal flow, *J. Geophys. Res.*, *96*, 8391–8405.

Gonnermann, H. M., M. Manga, and A. M. Jellinek (2002), Dynamics and longevity of an initially stratified mantle, *Geophys. Res. Lett.*, *29*(10), 1399, doi:10.1029/2003GC000583.

Griffiths, R. W., and I. H. Campbell (1990), Stirring and structure in mantle starting plumes, *Earth Planet. Sci. Lett.*, *99*, 66–78.

Gurnis, M. (1989), A reassessment of the heat transport by variable viscosity convection with plates and lids, *Geophys. Res. Lett.*, *16*, 179–182.

Jarvis, G. T. (1984), Time-dependent convection in the Earth's mantle, *Phys. Earth Planet. Inter.*, *36*, 305–327.

Jellinek, A. M., and M. Manga (2002), The influence of a chemical boundary layer on the fixity, spacing and lifetime of mantle plumes, *Nature*, *418*, 760–763.

Jellinek, A. M., H. M. Gonnermann, and M. A. Richards (2003), Plume capture by divergent plate motions: Implications for the distribution of hotspots, geochemistry of mid-ocean ridge basalts, and estimates of the heat flux at the core-mantle boundary, *Earth Planet. Sci. Lett.*, *205*, 361–378.

King, S. D. (1995), The viscosity structure of the mantle, *U.S. Natl. Rep. Int. Union Geod.*, *Geophys. 1991–1994 Rev. Geophys.*, *33*, 11–17.

King, S. D., and B. H. Hager (1990), The relationship between plate velocity and trench viscosity in Newtonian and power-law subduction calculations, *Geophys. Res. Lett.*, *17*, 2409–2412.

King, S. D., and G. Masters (1992), An inversion for radial viscosity structure using seismic tomography, *Geophys. Res. Lett.*, *19*, 1551–1554.

King, S. D., C. W. Gable, and S. A. Weinstein (1992), Models of convection-driven tectonic plates: A comparison of methods and results, *Geophys. J. Int.*, *109*, 481–487.

King, S. D., J. P. Lowman, and C. W. Gable (2002), Episodic tectonic plate reorganizations driven by mantle convection, *Earth Planet. Sci. Lett.*, *203*, 83–91.

Labrosse, S., J.-P. Poirier, and J.-L. Le Mouël (1997), On cooling of the Earth's core, *Phys. Earth Planet. Inter.*, *99*, 1–17.

Larsen, T. B., A. Yuen, and M. Storey (1999), Ultrafast mantle plumes and implications for flood basalt volcanism in the Northern Atlantic region, *Tectonophysics*, *311*, 31–43.

Lowman, J. P., S. D. King, and C. W. Gable (2001), The influence of tectonic plates on mantle convection patterns, temperature and heat flow, *Geophys. J. Int.*, *146*, 619–636.

Lowman, J. P., S. D. King, and C. W. Gable (2003), The role of the heating mode of the mantle in intermittent reorganization of the plate velocity field, *Geophys. J. Int.*, *152*, 455–467.

Mitrovica, J. X. (1996), Haskell (1935) revisited, *J. Geophys. Res.*, *101*, 555–569.

Mitrovica, J. X., and A. M. Forte (1997), Radial profile of mantle viscosity: Results from the joint inversion of convection and postglacial rebound observables, *J. Geophys. Res.*, *102*, 2751–2769.

Mitrovica, J. X., and A. M. Forte (2002), On the radial profile of mantle viscosity, in *Ice Sheets, Sea Level and the Dynamic Earth*, *Geodyn. Ser.*, vol. 29, pp. 187–199, AGU, Washington, D. C.

Molnar, P., and J. Stock (1987), Relative motions of hotspots in the Pacific, Atlantic and Indian oceans since late Cretaceous time, *Nature*, *327*, 587–591.

Monnereau, M., and S. Quéré (2001), Spherical shell models of mantle convection with tectonic plates, *Earth Planet. Sci. Lett.*, *184*, 575–587.

Morgan, J. W. (1971), Convection plumes in the lower mantle, *Nature*, *230*, 42–43.

Morgan, J. W. (1972), Plate motions and deep mantle convection, *Geol. Sci. Am. Man.*, *132*, 7–22.

Morgan, J. W. (1981), Hotspot tracks and the opening of the Atlantic and Indian oceans, in *The Sea*, vol. 7, edited by C. Emiliani, pp. 443–487, John Wiley, New York.

Puster, P., B. H. Hager, and T. H. Jordan (1995), Mantle convection experiments with evolving plates, *Geophys. Res. Lett.*, *22*, 2223–2226.

Richards, M. A., and R. W. Griffiths (1988), Deflection of plumes by mantle shear flow: Experimental results and a simple theory, *Geophys. J.*, *94*, 367–376.

Richards, M. A., and C. Lithgow-Bertelloni (1996), Plate motion changes, the Hawaiian-Emperor bend, and the apparent success and failure of geodynamic models, *Earth Planet. Sci. Lett.*, *137*, 19–27.

Richards, M. A., R. A. Duncan, and V. E. Courtillot (1989), Flood basalts and hot-spot tracks: Plume heads and tails, *Science*, *246*, 103–107.

Richards, M. A., H. P. Bunge, Y. Ricard, and J. R. Baumgardner (1999), Polar wandering in mantle convection models, *Geophys. Res. Lett.*, *26*, 1777–1780.

Schubert, G., D. L. Turcotte, and P. Olson (2001), *Mantle Convection in the Earth and Planets*, 940 pp., Cambridge Univ. Press, New York.

Steinberger, B. (2000), Plumes in a convecting mantle: Models and observations for individual hotspots, *J. Geophys. Res.*, *105*, 11,127–11,152.

Steinberger, B. M., and R. J. O'Connell (1997), Changes of the Earth's rotation axis owing to advection of mantle density heterogeneities, *Nature*, *387*, 169–173.

Steinberger, B. M., and R. J. O'Connell (1998), Advection of plumes in mantle flow: Implications for hotspot motion, mantle viscosity and plume distribution, *Geophys. J. Int.*, *132*, 412–434.

Tackley, P. J. (1998), Self-consistent generation of tectonic plates in three-dimensional mantle convection, *Earth Planet. Sci. Lett.*, *157*, 9–22.

Tackley, P. J. (2000), Mantle convection and plate tectonics: Toward an integrated physical and chemical theory, *Science*, *288*, 2002–2007.

Trompert, R., and U. Hansen (1998), Mantle convection simulations with rheologies that generate plate-like behaviour, *Nature*, *395*, 686–689.

Van den Berg, A. P., D. A. Yuen, and P. E. Van Keken (1991), Effects of depth variations on the formation of plates in mantle dynamics, *Geophys. Res. Lett.*, *18*, 2197–2200.

Van Keken, P. E., and C. W. Gable (1995), The interaction of a plume with a rheological boundary: A comparison between two- and three-dimensional models, *J. Geophys. Res.*, *100*, 20,291–20,302.

Van Keken, P. E., D. A. Yuen, and A. P. van den Berg (1992), Pulsating diapiric flows: Consequences of vertical variations in mantle creep laws, *Earth Planet. Sci. Lett.*, *112*, 179–194.

Weinstein, S. A., and P. L. Olson (1992), Thermal convection with non-Newtonian plates, *Geophys J. Int.*, *111*, 515–530.

Weinstein, S. A., P. L. Olson, and D. A. Yuen (1989), Time-dependent large aspect ratio thermal convection in the Earth's mantle, *Geophys. Astrophys. Fluid Dyn.*, *47*, 157–197.

Wessel, P., and L. W. Kroenke (2000), Ontong Java Plateau and late Neogene changes in Pacific Plate motion, *J. Geophys. Res.*, *105*, 28,255–28,277.

Wilson, J. T. (1963), Evidence from islands on the spreading of the ocean floor, *Nature*, *197*, 536–538.

Wilson, J. T. (1973), Mantle plumes and plate motions, *Tectonophysics*, *19*, 149–164.

Zhong, S., and M. Gurnis (1992), Viscous flow model of a subduction zone with a faulted lithosphere: Long and short wavelength topography, gravity, and geoid, *Geophys. Res. Lett.*, *19*, 1891–1894.

Zhong, S., and M. Gurnis (1995), Mantle convection with plates and mobile, faulted plate margins, *Science*, *267*, 838–843.

Zhong, S. J., M. Gurnis, and L. Moresi (1998), Role of faults, nonlinear rheology, and viscosity structure in generating plates from instantaneous mantle flow models, *J. Geophys. Res.*, *103*, 15,255–15,268.

Zhong, S., M. T. Zuber, L. Moresi, and M. Gurnis (2000), Role of temperature-dependent viscosity and surface plates in spherical shell models of mantle convection, *J. Geophys. Res.*, *105*, 11,063–11,082.